

1 Computational determination of a primary diffusion mode in
2 γ U-10Mo under irradiation

3 Gyuchul Park^a, Benjamin Beeler^{b,c}, Maria A. Okuniewski^{a,*}

4 ^a*School of Materials Engineering, Purdue University, West Lafayette, IN 47907, United States*

5 ^b*Department of Nuclear Engineering, North Carolina State University, Raleigh, NC 27695, United States*

6 ^c*Idaho National Laboratory, Idaho Falls, ID 83415, United States*

7 **Abstract**

Low enriched uranium ($< 20\% \ ^{235}\text{U}$)-molybdenum (U-Mo) monolithic fuel is the primary candidate for [..¹]high-performance research and test reactors [..²]and is in the process of being qualified to replace highly-enriched uranium ($\geq 20\% \ ^{235}\text{U}$) fuel. As part of the qualification process, it is critical to understand and predict the behavior of fission gas bubbles under irradiation, which affects fuel swelling and fuel failure. Mechanistic fuel models are being developed that can both reproduce the existing experimental data for fuel swelling, and be further applied to irradiation conditions beyond the experimental scope. Diffusion of species under irradiation conditions is an important parameter in the mechanistic fuel models; however, no temperature-relevant experimental diffusion data exists. In the present work, radiation-enhanced diffusion coefficients of U, Mo, and Xe in γ U-10wt.%Mo were calculated in the temperature range between 300 K and 1400 K via rate-theory models and molecular dynamics simulations with an embedded-atom method interatomic potential for the U-Mo-Xe system. Accordingly, total diffusion coefficients under relevant irradiation conditions are determined using previously obtained intrinsic thermal diffusion and radiation-driven diffusion coefficients, as well as the newly calculated radiation-enhanced diffusion coefficients presented herein. Radiation-enhanced diffusion of U and Mo was dominant in the intermediate temperature range, whereas radiation-enhanced diffusion of Xe did not significantly contribute to total diffusion of Xe at the relevant fission rate densities. Radiation-enhanced diffusion of Xe became faster than both intrinsic thermal diffusion and radiation-driven diffusion at a fission rate density of 5×10^{22} fissions/m³/s, which is higher than the typical fission rate density range in research reactors. The temperature regime [..³]where radiation-

*Corresponding author. Purdue University, West Lafayette, IN 47907, USA

Email address: mokuniew@purdue.edu (Maria A. Okuniewski)

¹removed: high performance

²removed: ,

³removed: that

enhanced diffusion of each element dominated was dependent on the fission rate density. The total diffusion coefficients of U, Mo, and Xe, updated in this work, will be utilized as parameters in the mechanistic fuel models to help predict the behavior of fission gas bubbles under irradiation more accurately.

- 8 *Keywords:* uranium-molybdenum (U-Mo) alloys, Xe, fission gas, intrinsic thermal
9 diffusion, radiation-enhanced diffusion, rate-theory model, molecular dynamics
-

10 **1. Introduction**

11 There are currently five [..⁴] **high-performance** research reactors (HPRR) and one criti-
12 cal assembly fueled by highly-enriched uranium (HEU, $\geq 20\% \text{ }^{235}\text{U}$) in the United States
13 (US): the Advanced Test Reactor and Advanced Test Reactor Critical Assembly at Idaho
14 National Laboratory, the High Flux Isotope Reactor at Oak Ridge National Laboratory, the
15 Massachusetts Institute of Technology Reactor, the National Bureau of Standards Reactor,
16 and the University of Missouri Research Reactor. Under the USHPRR program, initiated
17 and developed by the US Department of Energy and the Office of Material Management and
18 Minimization in the National Nuclear Security Administration, there have been substantial
19 efforts to convert HEU-based fuels to low enriched uranium (LEU, $< 20\% \text{ }^{235}\text{U}$) based fuels
20 to limit nuclear proliferation risks. LEU-molybdenum monolithic fuel was selected as a nu-
21 clear fuel material and design due to its high uranium density (17.3 g U/cm^3 for LEU-7Mo
22 monolithic fuel), dimensional stability, mechanical integrity, and stable swelling behavior at
23 high fission densities (up to $7.2 \times 10^{27} \text{ fissions/m}^3$) [1, 2, 3, 4, 5, 6]. LEU-10Mo monolithic
24 fuel is currently in the process of being experimentally tested and qualified to be utilized as
25 fuel for HPRRs [7, 8, 9].

26 Microstructural evolution of nuclear fuel under irradiation is a complicated process, in-
27 fluenced by a number of unique phenomena, ranging from the atomic scale to the microscale,
28 which affects the macroscopic properties of fuel. During reactor operation, an atom located
29 in a lattice can be removed from its lattice site [..⁵] **if it undergoes a collision with an energetic**
30 **particle and receives sufficient kinetic energy.** Primary knock-on atoms (PKAs) [..⁶] can create
31 secondary knock-on atoms which displace tertiary knock-on atoms, etc., ultimately resulting
32 in **the** creation of various types of defects such as interstitials, vacancies, dislocation loops,
33 and voids. This phenomenon, referred to as a displacement cascade, is the initiation point of
34 irradiation damage with a length-scale of nm and a time-scale of ps [10]. Noble gases such as

⁴removed: high performance

⁵removed: by a neutron having high enough

⁶removed: , knocked off by neutrons,

35 Xe and Kr, referred to as gaseous fission products, are also produced from the fission of ^{235}U
36 nuclei and have low solubility in the fuel matrix. The insoluble gaseous fission products tend
37 to coalesce and form fission gas bubbles through a diffusion process both inside the grains
38 (intragranular fission gas bubbles) and along the grain boundaries (intergranular fission gas
39 bubbles). In U-10Mo fuels, it was found that the intragranular fission gas bubbles were
40 considerably smaller than the intergranular fission gas bubbles [1, 11, 12]. The size of the
41 intergranular fission gas bubbles was a few hundreds of nm at a fission density of $2\text{-}3 \times 10^{27}$
42 fiss/m³ [1, 11], while the size of the intragranular fission gas bubbles was approximately 1-2
43 nm in diameter, and formed in a superlattice at a fission density of 1.41×10^{27} fiss/m³
44 [12]. Larger intragranular fission gas bubbles (3.5 nm in diameter) were observed at a higher
45 fission density of 4.5×10^{27} fiss/m³ [13], indicating that the size of the intragranular fission
46 gas bubbles grows slowly with increasing fission density. However, the intragranular fission
47 gas bubbles tend not to grow above a certain [..⁷]size due to re-solution [14]. The fission gas
48 bubbles are destroyed and re-solved through the interaction with energetic fission fragments,
49 and the re-solved fission gas atoms occupy the U-Mo body-centered cubic (bcc) lattice [14].
50 As fission density increases further, U-Mo fuel goes through grain refinement, historically
51 referred to as recrystallization, and provides additional nucleation sites for intergranular fis-
52 sion gas bubbles, thereby accelerating fuel swelling [15, 16, 17]. [..⁸]

53 Modeling and simulation play a pivotal role in understanding and predicting the mi-
54 crostructural evolution of fuel under irradiation conditions to facilitate fuel qualification.
55 For instance, the behavior of fission gas bubbles in U-Mo fuel under irradiation has been
56 studied primarily with phase-field models [20, 21, 22, 23]. In addition, U-Mo fuel swelling
57 mechanistic models, as implemented in the Dispersion Analysis Research Tool (DART) code,
58 are currently being developed to incorporate experimental observations and measurements,
59 thus enabling the prediction of U-Mo fuel swelling beyond the current experimental burn-up
60 regime [..⁹][24, 25]. Diffusion coefficients of the species in U-Mo under irradiation condi-
61 tions are critical parameters in the mechanistic fuel model; however, experimental data does
62 not exist at the relevant research reactor temperatures or under irradiation. This lack of
63 knowledge has motivated the current study of diffusion of the species (U, Mo, and Xe) in
64 $\gamma\text{U-10Mo}$ under irradiation conditions.

65 Turnbull et al. [26] reported that diffusion of fission gas in UO_2 under irradiation is
66 dominated by three different diffusion components depending on the temperature: intrinsic

⁷removed: level

⁸removed: Thus, the presence of the fission gas bubbles not only causes the degradation of thermal conductivity of fuel, but also facilitates fuel swelling, eventually resulting in fuel failure [18, 19].

⁹removed: [24]

67 thermal diffusion in the [..¹⁰]high-temperature regime (> 1600 K), radiation-enhanced diffusion
 68 in the intermediate temperature regime (between 1200 K and 1600 K), and radiation-
 69 driven diffusion in the [..¹¹]low-temperature regime (< 1200 K), at a fission rate density
 70 of 10^{19} fiss/m³/s. The intrinsic thermal diffusion is driven by the defect concentration at
 71 equilibrium. Intrinsic thermal diffusion of Xe in UO₂ [27], calculated via DFT calculations,
 72 agreed well with the experimental observations [..¹²][26]. Similar studies of U, Si, and Xe
 73 component-based diffusion have also been explored in U₃Si₂ accident tolerant fuel [28, 29].

74 To the best of the authors' knowledge, no Xe intrinsic thermal diffusion data in U-Mo fuel
 75 exists. For the purposes of lower length scale modeling, it has been initially assumed that the
 76 intrinsic thermal diffusion of Xe is slower than the intrinsic diffusion of U by approximately
 77 four orders of magnitude in γ U-Mo [21, 30, 31]. Intrinsic thermal diffusion of U and Mo in
 78 γ U-10Mo at research reactor temperatures can be extrapolated from [..¹³]high-temperature
 79 experiments (from 923 K to 1273K) by fitting the experimental data [32] into the determined
 80 Arrhenius equation. Thus, the accepted equations of intrinsic thermal diffusion (D_{INT} in
 81 m²/s) for U, Mo, and Xe in γ U-10Mo are as follows [21, 30, 31, 32]:

$$D_{INT}^U = 1.28 \times 10^{-5} \times \exp(-1.76/kT), \quad (1)$$

$$D_{INT}^{Mo} = 1.62 \times 10^{-5} \times \exp(-1.97/kT), \quad (2)$$

$$D_{INT}^{Xe^1} = 1.28 \times 10^{-9} \times \exp(-1.76/kT), \quad (3)$$

82 where k is the Boltzmann constant and T is the temperature in Kelvin (K).

83 Radiation-driven diffusion, controlled by ballistic mixing due to collision cascades, was
 84 previously found to be athermal and dependent on the fission fragment kinetic energy from
 85 a single fission event and the associated species' mean-squared displacements, which are
 86 dependent on the PKA energy density [..¹⁴][29]. It should be noted that defects can be
 87 also produced via not only collision cascades, but also the transfer of energy deposited by fission
 88 fragments into the electronic subsystem (thermal spike) [34, 35]. It was assumed that the effects

¹⁰removed: high temperature

¹¹removed: low temperature

¹²removed: [26?]

¹³removed: high temperature

¹⁴removed: . Radiation-driven diffusion of Xe was faster than radiation-driven diffusion of U in UO₂, whereas radiation-driven diffusion of Xe was faster than radiation-driven diffusion of U and Mo in γ U-10Mo [29, 33]. This is presumed to be due to localized melting from

⁸⁹ of the thermal spike [..¹⁵] were negligible. Radiation-driven diffusion (D_{RDD} in m^2/s) of U,
⁹⁰ Mo, and Xe in $\gamma\text{U}-10\text{Mo}$, calculated by Beeler et al. [29], is described as follows:

$$D_{RDD}^U = 1.97 \times 10^{-41} \times \dot{F}, \quad (4)$$

$$D_{RDD}^{Mo} = 2.01 \times 10^{-41} \times \dot{F}, \quad (5)$$

$$D_{RDD}^{Xe} = 5.07 \times 10^{-41} \times \dot{F}, \quad (6)$$

⁹¹ where \dot{F} is the fission rate density in $\text{fiss}/\text{m}^3/\text{s}$.

⁹² Radiation-enhanced diffusion is governed by enhanced defect concentrations under irra-
⁹³ diation. Radiation-enhanced diffusion in UO_2 and U_3Si_2 was investigated through cluster
⁹⁴ dynamics calculations parametrized by DFT calculations and MD simulations [27, 36, 37].
⁹⁵ Radiation-enhanced diffusion coefficients of species in $\gamma\text{U}-\text{Mo}$ do not exist, which has moti-
⁹⁶ vated the current study.

⁹⁷ In this work, the radiation-enhanced diffusion (D_{RED}) of U, Mo, and Xe [..¹⁶] is deter-
⁹⁸ mined utilizing a rate-theory model parametrized using MD simulations. Intrinsic thermal
⁹⁹ diffusion of Xe in $\gamma\text{U}-10\text{Mo}$ is additionally determined using MD simulations with the as-
¹⁰⁰ sumption that Xe diffusion is facilitated by a vacancy. The total diffusion coefficients (D_{TOT})
¹⁰¹ of U, Mo, and Xe in $\gamma\text{U}-\text{Mo}$ under irradiation conditions are also presented as a summation
¹⁰² of the three diffusion components, given in Eqn. 7, in the temperature range between 300
¹⁰³ K and 1400 K and in the fission rate density range between 5×10^{18} $\text{fiss}/\text{m}^3/\text{s}$ and 5×10^{22}
¹⁰⁴ $\text{fiss}/\text{m}^3/\text{s}$.

$$D_{TOT} = D_{INT} + D_{RED} + D_{RDD}. \quad (7)$$

¹⁰⁵ 2. Computational Details

¹⁰⁶ 2.1. Interatomic Potential

¹⁰⁷ Molecular dynamics is a simulation method capable of generating the trajectory of atoms
¹⁰⁸ (or molecules) in a given system. The force acting on each atom can be calculated by numer-
¹⁰⁹ ically integrating Newton's equations of motion with the initial positions and velocities of
¹¹⁰ atoms in the system. The reliability of MD simulations is highly dependent on the accuracy

¹⁵removed: during the displacement cascade, where Xe is able to diffuse in liquid UO_2 and $\gamma\text{U}-10\text{Mo}$ rapidly [29, 33]

¹⁶removed: ,

111 of the interatomic potential utilized. In this work, an embedded-atom method (EAM) inter-
112 atomic potential was used to perform MD simulations with the LAMMPS software package
113 [38]. The accuracy of the EAM formalism comes from its description of many-body interac-
114 tions, which does not exist within pairwise potentials.

115 A general form of the EAM interatomic potential, developed by Daw and Baskes, is
116 described as follows [39, 40]:

$$E_T = [\dots^{17}] \sum_{i < j} \phi_{ij}(r_{ij}) + \sum_i F\left(\sum_{j \neq i} \rho_i(r_{ij})\right), \quad (8)$$

117 where E_T is the total energy of the system, ϕ_{ij} is the pair potential function, which is depen-
118 dent on the distance (r_{ij}) between the two given atoms i and j . The term F is the embedding
119 energy of atom i , which depends on the spatially-dependent electron density and determines
120 the many-body interatomic interactions. Each atom is regarded as being embedded in the
121 background electron density, and the electron density is dependent on the neighboring atoms.
122 In this work, the EAM potential for the ternary U-Mo-Xe system, developed by Smirnova
123 et al. [41], was used. This potential was fitted to the first principles data including forces
124 and energies using the force-matching method [42]. The U-Mo-Xe ternary EAM interatomic
125 potential was chosen in this work since the material properties, including the lattice param-
126 eter, thermal expansion coefficient, Young's modulus, and melting temperature of U-10Mo
127 alloys were in agreement with the experimental observations [41]. Additionally, this is the
128 only interatomic potential **currently available** that describes the ternary U-Mo-Xe system.

129 *2.2. $[\dots^{18}]$ Atomistic modeling of the diffusion of U, Mo, and Xe*

130 A supercell of 10 x 10 x 10 unit cells (2,000 atoms) of γ U was created with periodic
131 boundary conditions. Such a relatively large supercell was utilized to produce the random
132 substitutional solid solution alloys and to avoid the interaction of the Xe-vacancy clusters
133 across periodic boundary conditions. Twenty-three percent of the U atoms were replaced
134 with Mo atoms, corresponding to a 10 wt.% bcc random solid substitutional alloy. The sys-
135 tem was relaxed for 200 ps with a timestep of 0.002 ps in an NPT ensemble with a Langevin
136 thermostat in the Gronbech-Jenson-Farago formalism [43, 44]. This has been previously
137 identified to be more than sufficient for the appropriate relaxation of such a system [45].
138 Subsequently, a defect (vacancy/self-interstitial/Xe-vacancy cluster) was separately created
139 in the system, and the system was relaxed for another 200 ps. Xe diffusion in $[\dots^{19}]$ U-Mo was
140 based on the assumption that Xe diffuses via vacancy clustering, as observed in other fuel

¹⁸removed: Diffusion Coefficient

¹⁹removed: UMo

materials [27, 46, 47, 48, 49]. Interstitial diffusion is not considered in the calculations of the radiation-enhanced diffusion of Xe. The formation energy of a Xe interstitial atom is greater than the summation of the formation energy of substitutional Xe atom and self-interstitial atom (U or Mo) in γ U-10Mo [50, 51, 52]. Additionally, the energetics of Xe defects [..²⁰] dictated that Xe interstitials will generate a self-interstitial and reside as a substitutional atom, providing justification for neglecting an interstitial mechanism [..²¹][50, 51, 52]. Due to the extremely slow diffusion of Xe, the diffusion coefficient of Xe in a vacancy cluster was calculated with respect to the vacancy cluster size. The schematics of the Xe-vacancy cluster arrangements in γ U-10Mo considered in this work are represented in Fig. 1. The atomic positions of both U and Mo atoms surrounding a Xe atom, randomly distributed in a substitutional manner in a bcc lattice, were considered vacant sites. Vacancy and interstitial diffusion coefficients of U and Mo ($D_{v/i}^{U/Mo}$), and the diffusion coefficient of Xe in a vacancy cluster (D_{nvac}^{Xe}) were calculated with the slope of the mean-squared displacement with time as follows:

154

$$D_{v/i/nvac}^{U/Mo/Xe} = \frac{\sum_{i=1}^N \langle \Delta r_i^2 \rangle}{6t}, \quad (9)$$

[..²⁴]

155

where $\langle \Delta r_i^2 \rangle$ is the mean-squared displacement of the i^{th} atom [..²⁵] and t is the simulation time. The mean-squared displacements of U and Mo in the system were obtained for 100 ns. Since the diffusion of Xe was extremely slow when compared to U and Mo in the temperature regime investigated, a longer time period of 500 ns was required. Twenty simulations were conducted from 800 K to 1400 K for U and Mo, and from 1000 K to 1400 K for Xe. The obtained diffusion coefficients were averaged.

162 2.3. Steady-State Defect Concentration under Irradiation

The steady-state concentration of vacancies and interstitials under irradiation conditions can be obtained by solving the coupled differential equations as follows:

²⁰removed: dictates

²¹removed: [50, 51]. It should be noted that due

²⁵removed: ,

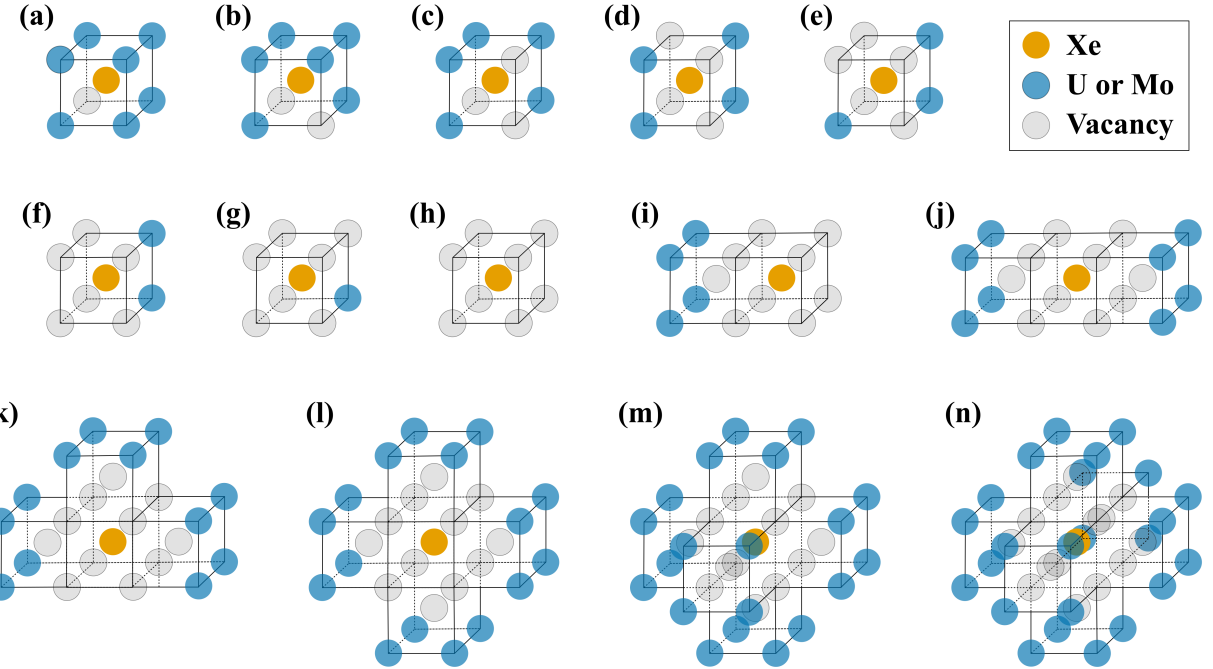


Figure 1: Schematics of the Xe-vacancy clusters in γ U-10Mo considered in the present work: (a) Xe-monovacancy ($n=1$), (b) Xe-divacancy ($n=2$), (c) Xe-trivacancy ($n=3$), (d) Xe-quadvacancy ($n=4$), (e) Xe-pentavacancy ($n=5$), (f) Xe-hexavacancy ($n=6$), (g) Xe-heptavacancy ($n=7$), (h) Xe-octavacancy ($n=8$), (i) Xe-nonavacancy ($n=9$), (j) Xe-decavacancy ($n=10$), (k) Xe-undecavacancy ($n=11$), (l) Xe-dodecavacancy ($n=12$), (m) Xe-tridecavacancy ($n=13$), and (n) Xe-tetradecavacancy ($n=14$), where n is the number of vacancies in a Xe cluster. Blue spheres represent the matrix U-Mo, yellow spheres represent Xe, and grey spheres represent vacant sites.

$$\frac{dC_v}{dt} = \epsilon \dot{F} - K_{iv} C_i C_v - k_{vs}^2 D_v C_v, \quad (10)$$

$$\frac{dC_i}{dt} = \epsilon \dot{F} - K_{iv} C_i C_v - k_{is}^2 D_i C_i, \quad (11)$$

where C_v is the concentration of vacancies^{[..²⁶], C_i is the concentration of interstitials^{[..²⁷], ϵ is the defect production rate per fission event, K_{iv} is the recombination rate constant between vacancies and interstitials, k_{vs}^2 is the sink strength of grain boundaries for vacancies, k_{is}^2 is the sink strength of grain boundaries for interstitial atoms, D_v is the vacancy diffusion coefficient, and D_i is the interstitial diffusion coefficient. Sinks were restricted to grain boundaries in this work (e.g., dislocation sinks were neglected). The coupled differential equations were solved using the Rosenbrock solver (Rodas-4) with Julia [53, 54].}}

²⁶removed: at equilibrium

²⁷removed: at equilibrium, \dot{F} is the fission rate density,

¹⁷² The defect production rate (ϵ) was calculated from the athermal recombination corrected
¹⁷³ dpa (arc-dpa) model [55], which is a modification of the NRT dpa model [56] which calcu-
¹⁷⁴ lates the number of atomic displacements. The arc-dpa model takes into account thermally
¹⁷⁵ activated recombination, resulting in a decrease in the number of defects existing under ir-
¹⁷⁶ radiation as compared to the NRT dpa model [55]. The number of defects generated (N_d) is
¹⁷⁷ described by the arc-dpa model as:

¹⁷⁸

$$N_d = \frac{0.8T_d}{2E_d}\xi, \quad (12)$$

¹⁷⁹

¹⁸⁰ where T_d is the damage energy, E_d is the threshold displacement energy, and ξ is the arc-dpa
¹⁸¹ efficiency function [55]. The damage energy is taken as the kinetic energy of the fission frag-
¹⁸² ments produced from a fission reaction (approximately 170 MeV), and reduced to account
¹⁸³ for electronic energy losses. It is assumed that only ballistic effects generate Frenkel pairs.
¹⁸⁴ The electronic energy losses have been previously calculated to be 95%, thus the damage
¹⁸⁵ energy used is 8.5 MeV [29]. The magnitude of the threshold displacement energy for γ U-
¹⁸⁶ 10Mo is not well known, but can potentially be determined from MD simulations or from
¹⁸⁷ experiments. Given that such studies are beyond the scope of this work, reasonable approxi-
¹⁸⁸ mations are made for the threshold displacement energy (60 eV) based upon MD simulations
¹⁸⁹ in γ U [57], and for the arc-dpa efficiency (0.25), which is approximately the same as bcc Fe
¹⁹⁰ [55]. This yields approximately 14,000 point defects per fission event in γ U-10Mo. The
¹⁹¹ defect production rate was obtained by dividing the number of generated defects per fission
¹⁹² event by the atomic number density of γ U-10Mo. ^[..²⁸] Any bias towards interstitial atoms
¹⁹³ or vacancies in the defect production process is neglected, assuming that an equal number
¹⁹⁴ of both types of defects are generated. **The number of point defects generated in a fission**
¹⁹⁵ **event for this work utilized calculations from Beeler et al. [29], which generally agreed with the**
¹⁹⁶ **estimates from Kolotova et al. [35].**

¹⁹⁷ In order to determine the recombination rate constant (K_{iv}), separate MD simulations
¹⁹⁸ were conducted. A supercell of 40 x 40 x 40 unit cells (128,000 atoms) of γ U was generated
¹⁹⁹ with an atomic composition of 10 wt.% of Mo with periodic boundary conditions. Fifty
²⁰⁰ Frenkel pairs were created, ensuring that the distance between individual defects is at least
²⁰¹ $4a_0$, where a_0 is the lattice constant. The system was equilibrated for 20,000 timesteps with
²⁰² a variable timestep such that a maximum distance for an atom to move in one timestep is
²⁰³ 5 fm, in order to perform a constrained relaxation of the defects. Subsequently, the system

²⁸removed: It should be noted that any

204 was evolved for 10 ns with a timestep of 1 fs, tracking the number of Frenkel pairs as a
205 function of time via the Voronoi occupation methodology within the LAMMPS. This com-
206 putational setup is in line with previous efforts to determine recombination rate constants
207 utilizing MD [58]. This defect evolution simulation was performed from 600 K to 1200 K
208 in increments of 100 K. For a given temperature, the number of defects (C_0) as a function
209 of time can be fit to $C = C_0/(C_0 K_{iv} t + 1)$, where C_0 is the initial concentration of Frenkel
210 pairs. In classical rate theory, the grain boundaries are constant sinks and their strength,
211 k^2 , is estimated as $15/L^2$ (L is the grain size, in units of nm) for grain boundaries with a
212 regular pattern, and is identical for both interstitials and vacancies. This assumption is uti-
213 lized here as a first approximation, and along with a grain size estimate of 10 μm , completes
214 the parameterization of the rate theory equations. The grain size is defined as the aver-
215 age diameter of the grains. It should be noted that the steady-state concentration of defects
216 increased with increasing grain size, and saturated when the grain size was greater than 1 μm .

217

218 2.4. Xe-Vacancy Cluster Concentration under Irradiation

219 A separate rate-theory formulation was constructed with the assumption that Xe, the
220 most common fission product [59], was continuously produced in the system, and thus Xe-
221 vacancy clusters with various sizes were also present. Xe-vacancy clusters containing up to
222 fourteen vacancies were taken into account, as mentioned previously. For instance, the first
223 and second nearest neighbor shells are completely composed of vacancies near a Xe atom
224 within a bcc lattice in a Xe-tetravacancy cluster ($n=14$). The rate of change in defect con-
225 centrations including Xe and Xe-vacancy clusters with time can be mathematically described
226 as follows:

$$\frac{dC_v}{dt} = \epsilon \dot{F} - K_{iv} C_i C_v - k_{vs}^2 D_v C_v \quad (13)$$

$$+ \sum_{n=1}^{14} \alpha_{n+1} C_{Xe-nv} - \sum_{n=1}^{13} \beta_n C_v C_{Xe-(n-1)v} + \sum_{n=1}^{13} n R C_{Xe-nv},$$

$$\frac{dC_i}{dt} = \epsilon \dot{F} - K_{iv} C_i C_v - k_{is}^2 D_i C_i, \quad (14)$$

$$\frac{dC_{Xe}}{dt} = \tau \dot{F} - \beta_1 C_v C_{Xe} + \alpha_2 C_{Xe-1v} + \sum_{n=1}^{14} R C_{Xe-nv}, \quad (15)$$

$$\frac{dC_{Xe-1v}}{dt} = \beta_1 C_v C_{Xe} - \beta_2 C_v C_{Xe-1v} - \alpha_2 C_{Xe-1v} + \alpha_3 C_{Xe-2v} - R C_{Xe-1v}, \quad (16)$$

$$\frac{dC_{Xe-2v}}{dt} = \beta_2 C_v C_{Xe-1v} - \beta_3 C_v C_{Xe-2v} - \alpha_3 C_{Xe-2v} + \alpha_4 C_{Xe-3v} - R C_{Xe-2v}, \quad (17)$$

$$\frac{dC_{Xe-3v}}{dt} = \beta_3 C_v C_{Xe-2v} - \beta_4 C_v C_{Xe-3v} - \alpha_4 C_{Xe-3v} + \alpha_5 C_{Xe-4v} - R C_{Xe-3v}, \quad (18)$$

⋮

$$\frac{dC_{Xe-14v}}{dt} = \beta_{14} C_v C_{Xe-13v} - \alpha_{15} C_{Xe-14v} - R C_{Xe-14v}, \quad (19)$$

227 where C_{Xe} is the Xe concentration[..²⁹], C_{Xe-nv} is the concentration of a Xe cluster con-
 228 taining n vacancies[..³⁰], τ is the yield of Xe from fission reactions where $\tau = 0.13$ [60],
 229 β_n is the absorption coefficient, α_n is the emission coefficient, and R is the re-solution rate
 230 of a Xe-vacancy cluster where $R = 2.0 \times 10^{-24}$ [..³¹] $\times \dot{F}$ (s^{-1}) [61]. The absorption and
 231 emission coefficients were calculated by Eqns. 20 and 21 [62]:

232

$$\beta_n = \frac{4\pi(r_0 + r_n)D_v}{V_{at}}, \quad (20)$$

$$\alpha_{n+1} = \beta_n \exp\left(\frac{-E_n^b}{kT}\right), \quad (21)$$

233

234 where r_0 is the radius of a single vacancy, r_n is the radius of a Xe-vacancy cluster containing
 235 n vacancies, and E_n^b is the binding energy of the n^{th} vacancy in a Xe cluster containing n
 236 vacancies. Assuming all clusters are spherical, $r_n = (\frac{3nV_{at}}{4\pi})^{1/3}$, where V_{at} is the volume per

²⁹removed: at steady-state

³⁰removed: at steady-state

³¹removed: m³

²³⁷ atom for the bcc crystal structure, given by $V_{at} = \frac{a_0^3}{2}$. The binding energy of the n^{th} vacancy
²³⁸ in a Xe cluster containing n vacancies (E_n^b) was calculated as in Eqn. 22:

²³⁹

$$E_n^b = E_{Xe-(n+1)vac}^f - E_{Xe-nvac}^f - E_v^f, \quad (22)$$

²⁴⁰

²⁴¹ where $E_{Xe-nvac}^f$ is the formation energy of a Xe cluster containing n vacancies, $E_{Xe-(n+1)vac}^f$
²⁴² is the formation energy of a Xe cluster containing $n+1$ vacancies, and E_v^f is the vacancy
²⁴³ formation energy. The vacancy formation energy in γ U-10Mo was assumed to be 1.6 eV
²⁴⁴ [52].^[..³²]

²⁴⁵ Separate MD simulations were also performed to calculate the formation energies of a Xe-
²⁴⁶ vacancy cluster in γ U-10Mo. A supercell of $10 \times 10 \times 10$ unit cells of γ U was created with
²⁴⁷ periodic boundary conditions. Twenty-three percent of the U atoms in the system were sub-
²⁴⁸ stituted by Mo atoms to produce γ U-10Mo. The system was equilibrated for 200 ps at the
²⁴⁹ evaluated temperatures (from 400 K to 1400 K in increments of 200 K) in an NPT ensemble
²⁵⁰ with a Langevin thermostat in the Gronbech-Jenson-Farago formalism [43, 44] with a timestep
²⁵¹ of 0.002 ps. Subsequently, various sizes of the Xe-vacancy clusters were created in the system
²⁵² separately (Fig. 1), and the system was equilibrated for another 200 ps. The formation energies
²⁵³ of a Xe cluster containing n and $n+1$ vacancies ($E_{Xe-nvac}^f$ and $E_{Xe-(n+1)vac}^f$) were calculated
²⁵⁴ as in Eqns. 23 and 24:

²⁵⁵

$$E_{Xe-nvac}^f = E_{Xe-nvac} - \frac{\{N - (n + 1)\}}{N} E_{ideal}, \quad (23)$$

$$E_{Xe-(n+1)vac}^f = E_{Xe-(n+1)vac} - \frac{\{N - (n + 2)\}}{N} E_{ideal}, \quad (24)$$

²⁵⁶

²⁵⁷ where E_{ideal} is the potential energy of the system containing no defects, $E_{Xe-nvac}$ is the po-
²⁵⁸ tential energy of the system containing a Xe cluster with n vacancies, $E_{Xe-(n+1)vac}$ is the
²⁵⁹ potential energy of the system containing a Xe cluster with $n+1$ vacancies, and N is the
²⁶⁰ number of atoms in the system. Numerous simulations were conducted until the cumulative
²⁶¹ moving average of the potential energy of each system converged **to consider different con-**
²⁶² **figurational environments (U and Mo) in the alloy** [45]. Thus, two hundred simulations were
²⁶³ performed, and the potential energies were averaged at each temperature.

³²removed: The

264

265 *2.5. Radiation-enhanced Diffusion of U, Mo, and Xe in γ U-10Mo*

266 Given a steady-state concentration of vacancies and interstitials under irradiation and the
 267 diffusion coefficients of vacancies and interstitials, the radiation-enhanced diffusion coefficient
 268 (D_{RED}) of U and Mo can be expressed as follows [63]:

$$D_{RED}^U = D_v^U C_v^{irr} + D_i^U C_i^{irr}, \quad (25)$$

$$D_{RED}^{Mo} = D_v^{Mo} C_v^{irr} + D_i^{Mo} C_i^{irr}, \quad (26)$$

269

270 where D_v^U is the vacancy diffusion coefficient of U, D_v^{Mo} is the vacancy diffusion coefficient
 271 of Mo, D_i^U is the interstitial diffusion coefficient of U, D_i^{Mo} is the [..³³] interstitial diffusion
 272 coefficient of Mo, C_v^{irr} is the steady-state concentration of [..³⁴] vacancies under irradiation,
 273 and C_i^{irr} is the steady-state concentration of interstitials under irradiation. Unlike U and
 274 Mo, it is assumed that the diffusion of Xe occurs through vacancy clustering, and thus the
 275 radiation-enhanced diffusion coefficient of Xe can be described as follows [63]:

276

$$D_{RED}^{Xe} = \sum_{n=1}^{..35^{k-1}} D_{nvac}^{Xe} C_{Xe-nvac}^{irr}, \quad (27)$$

277

278 where and $C_{Xe-nvac}^{irr}$ is the concentration of a Xe cluster containing n vacancies under irra-
 279 diation. It was assumed that Xe-vacancy clusters do not interact with each other. As will be
 280 discussed, in order to approximate losses to large bubbles, the largest Xe-vacancy clusters are
 281 considered immobile.

282 *2.6. Intrinsic Thermal Diffusion of Xe in γ U-10Mo*

283 The intrinsic thermal diffusion coefficient of Xe in γ U-10Mo was also calculated since
 284 both experimental and computational data do not exist. In addition, the [..³⁶] previously uti-
 285 lized value of the intrinsic thermal diffusion coefficient of Xe is based on the hypothesis that
 286 the intrinsic thermal diffusion of Xe is slower than that of U by four orders of magnitude [21].
 287 With the assumption that [..³⁷] diffusion of Xe is mediated by a vacancy [27, 46, 47, 48, 49],

³³removed: intersitial

³⁴removed: vacancices

³⁶removed: published

³⁷removed: Xe diffuses through vacancy clustering

²⁸⁸ the intrinsic thermal diffusion of Xe ($D_{INT}^{Xe^2}$) can be calculated under the same computational
²⁸⁹ parameters described in Section 2.2 as follows:

²⁹⁰

$$D_{INT}^{Xe^2} = c_v D_{1vac}^{Xe}, \quad (28)$$

²⁹¹

²⁹² where c_v is the vacancy concentration at equilibrium and D_{1vac}^{Xe} is the diffusion coefficient of
²⁹³ Xe in a mono-vacancy cluster. The concentration of vacancies at equilibrium was calculated
²⁹⁴ using the equation as follows:

$$c_v = \exp\left(\frac{\Delta S_v^f}{k_B}\right) \exp\left(\frac{-E_v^f}{k_B T}\right), \quad (29)$$

²⁹⁵ where ΔS_v^f is the change in entropy introduced from creating a vacancy. The equilibrium
²⁹⁶ vacancy concentration is not affected by the entropy term, as has been previously assumed
²⁹⁷ in diffusional studies in γ U-Mo [45, 64].

²⁹⁸ 3. Results

²⁹⁹ 3.1. Recombination Rate Constant

³⁰⁰ The number of defects ^[..³⁸]was determined as a function of time in the temperature
³⁰¹ range between 600 K and 1200 K in increments of 100 K. Fig. 2(a) represents the defect
³⁰² concentration with respect to time in γ [..³⁹]U-10Mo at 1000 K, as an example. Temperatures
³⁰³ below 600 K were not explored, as intrinsic diffusion on MD timescales is very limited below
³⁰⁴ 600 K in γ U-10Mo. It can be observed that the number of defects decays as a function of
³⁰⁵ time in a near-exponential fashion, with the rate of annihilation slowing as a function of
³⁰⁶ time due to the decreased number of defects present. The fit to the data is also shown in
³⁰⁷ Fig. 2(a), which provides a value of the recombination rate constant (K_{iv}) at 1000 K. For
³⁰⁸ each individual temperature analyzed, the recombination rate constant is calculated from
³⁰⁹ the defect concentration as a function of time. Fig. 2(b) represents the recombination rate
³¹⁰ constant from 600 K to 1200 K along with the power function fit.

³¹¹ According to kinetic theory [63], the recombination rate constant can be estimated as
³¹² $K_{iv} = 4\pi(D_v + D_i)r_{iv}/V_{at}$, where r_{iv} is the interstitial-vacancy recombination radius. Typical
³¹³ values of the recombination radius are on the order of 2-3 times the equilibrium lattice
³¹⁴ constant (a_0) [65, 66]. By utilizing the fit values of the recombination rate constant and
³¹⁵ the known diffusion coefficients and equilibrium volume, the recombination radius can be

³⁸removed: were

³⁹removed: U-Mo

³¹⁶ determined. It is found that ^{[..⁴⁰]the} recombination radius is significantly larger than what
³¹⁷ is typically observed. For example, at 1000 K, the recombination radius is approximately
³¹⁸ $8a_0$. As the temperature decreases, the recombination radius increases farther, such that
³¹⁹ the distance of the recombination radius at 600 K is $24a_0$. **Considerably larger recombination**
³²⁰ **radii ($3.5\text{--}15a_0$) were also observed in UO_2 , which is in agreement with the present work [67].**
³²¹ It is assumed that this is due to the long stress field interactions between interstitials and
³²² vacancies, leading to rapid recombination. This perhaps compensates for the low interstitial
³²³ formation energies in γU systems, such that the large number of defects that are created can
³²⁴ also rapidly recombine. Such a phenomenon was hinted at in previous studies of displacement
³²⁵ energies in γU [57].

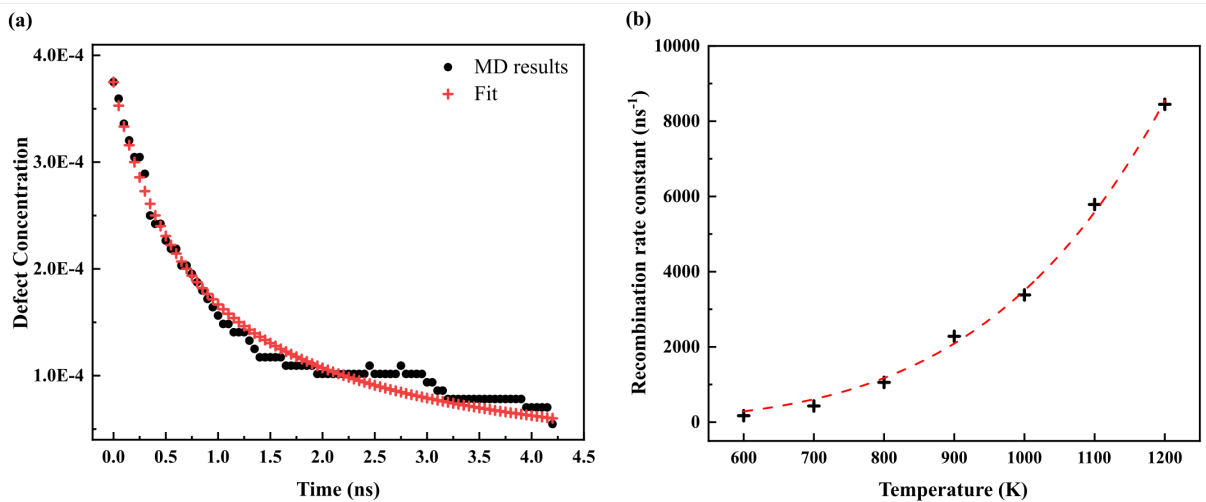


Figure 2: (a) The evolution of Frenkel pair concentration as a function of time at 1000 K, accounting for recombination. (b) Recombination rate constants (K_{iv}) as a function of temperature.

³²⁶ 3.2. Radiation-enhanced Diffusion of U and Mo

³²⁷ Implementing the recombination rate constant from Section 3.1, Eqns. 10 and 11 are used
³²⁸ to determine the steady-state concentration of point defects under irradiation as a function
³²⁹ of <sup>[..⁴¹]temperature in $\gamma\text{U-10Mo}$ at three different fission rate densities. Fig. 3(a) shows
³³⁰ the evolution of the concentration of vacancies and interstitials at the fission rate density of
³³¹ $5 \times 10^{20} \text{ fiss}/\text{m}^3/\text{s}$ at 1000 K, as an example. It took approximately 0.2 s for the concentra-
³³² tion of both vacancies and interstitials to reach steady-state under these conditions. **With**
³³³ **decreasing temperature, it takes longer for the concentrations of vacancies and interstitials to**
³³⁴ **reach the steady-state, as expected.** The steady-state concentrations of vacancies and inter-</sup>

⁴⁰removed: that

⁴¹removed: fission rate density and

stitals as a function of [..⁴²] temperature are shown at three different fission rate densities in Fig. 3(b). As the temperature increases, the number of vacancies and interstitials recombining increases, resulting in a decrease in the steady-state concentration of vacancies and interstitials. The concentration of vacancies was higher than the concentration of interstitials since the interstitials, which diffuse faster than vacancies, diffused into sinks such as grain boundaries [45, 68]. The concentration of vacancies decreased more rapidly than the concentration of interstitials with increasing temperature. This implies that the diffusion of vacancies is more sensitive to temperature than the diffusion of interstitials.

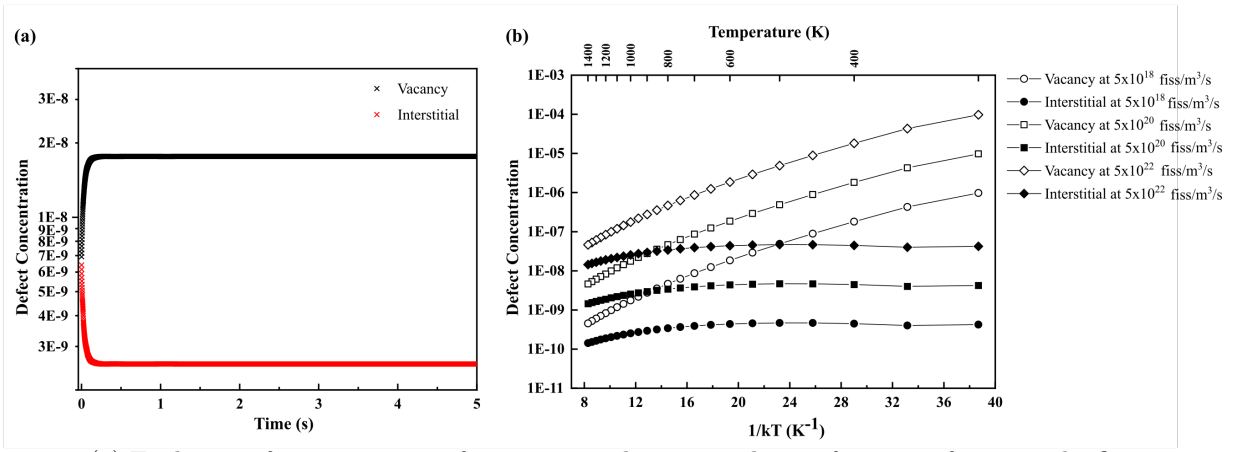


Figure 3: (a) Evolution of concentration of vacancies and interstitials as a function of time at the fission rate density of 5×10^{20} fiss/m³/s at 1000 K, as an example. (b) Rate theory calculations of the defect concentration evolution as a function of inverse temperature at three fission rate densities (units are fiss/m³/s). Note that the y-axis is shown in a log scale.

Fig. 4(a) shows the vacancy and interstitial diffusion coefficients of U and Mo in γ U-10Mo as a function of [..⁴³] temperature. The calculated diffusion coefficients were extrapolated to lower temperatures by fitting to an Arrhenius equation. The calculation of vacancy and interstitial diffusion of U and Mo (D_v^U , D_i^U , D_v^{Mo} , and D_i^{Mo}) in γ U-10Mo was previously conducted by the authors [45], and additional MD calculations were conducted at 900 K, 1100 K, 1300 K, and 1400 K to improve statistics within this work. The diffusion via interstitial atoms was faster than diffusion via vacancies in the evaluated temperature range, indicating that the diffusion in γ U-10Mo takes place primarily via interstitial atoms [45, 68]. Vacancy and interstitial diffusion of U and Mo ($D_v^{U/Mo}$ and $D_i^{U/Mo}$) were insignificant below 900 K and 800 K, respectively, within the MD timescales. The results of the Arrhenius fits for vacancy and interstitial diffusion of U and Mo are given in Table 1.

Using the steady-state concentration of vacancies and interstitials, as well as the diffusion

⁴²removed: inverse

⁴³removed: inverse

355 coefficients of vacancies and interstitials, the radiation-enhanced diffusion coefficients of U
 356 and Mo in γ U-10Mo were calculated, as shown in Fig. 4(b), as a function of [..⁴⁴] temper-
 357 ature at three fission rate densities. The radiation-enhanced diffusion of U was found to be
 358 faster than that of Mo, originating from the higher interstitial diffusion coefficient of U. The
 359 effect of the fission rate density on radiation-enhanced diffusion of U and Mo was evaluated,
 360 and a square root dependence of the radiation-enhanced diffusion coefficient was observed,
 361 as expected [28, 37]. A coefficient for fission-rate dependence can be obtained by dividing
 362 the total radiation-enhanced diffusion by the square root of the fission rate density. Thus,
 363 the [..⁴⁵] total diffusion coefficients of U and Mo [..⁴⁶] in γ U-10Mo[..⁴⁷], respectively, under
 364 irradiation can be obtained by the summation of intrinsic thermal diffusion, radiation-enhanced
 365 diffusion, and radiation-driven diffusion as follows:
 366

[..⁴⁸]

$$D_U = 1.28 \times 10^{-5} \times \exp\left(-\frac{1.76}{kT}\right) + 1.10 \times 10^{-26} \times \exp\left(-\frac{0.38}{kT}\right) \times \sqrt{\dot{F}} + 1.97 \times 10^{-41} \times \dot{F}, \quad (30)$$

[..⁴⁹]

$$D_{Mo} = 1.62 \times 10^{-5} \times \exp\left(-\frac{1.97}{kT}\right) + 2.10 \times 10^{-27} \times \exp\left(-\frac{0.39}{kT}\right) \times \sqrt{\dot{F}} + 2.01 \times 10^{-41} \times \dot{F}. \quad (31)$$

368

369

370 Radiation-enhanced diffusion of U and Mo in γ U-10Mo is displayed alongside intrinsic
 371 [..⁵⁰] diffusion and radiation-driven diffusion as a function of inverse temperature at three
 372 fission rate densities in Fig. 5 (a)-(c) and Fig. 6 (a)-(c), respectively. [..⁵¹] Intrinsic dif-

⁴⁴removed: inverse

⁴⁵removed: radiation-enhanced

⁴⁶removed: ($D_{RED}^{U/Mo}$)

⁴⁷removed: are as described below

⁵⁰removed: thermal

⁵¹removed: Radiation-enhanced

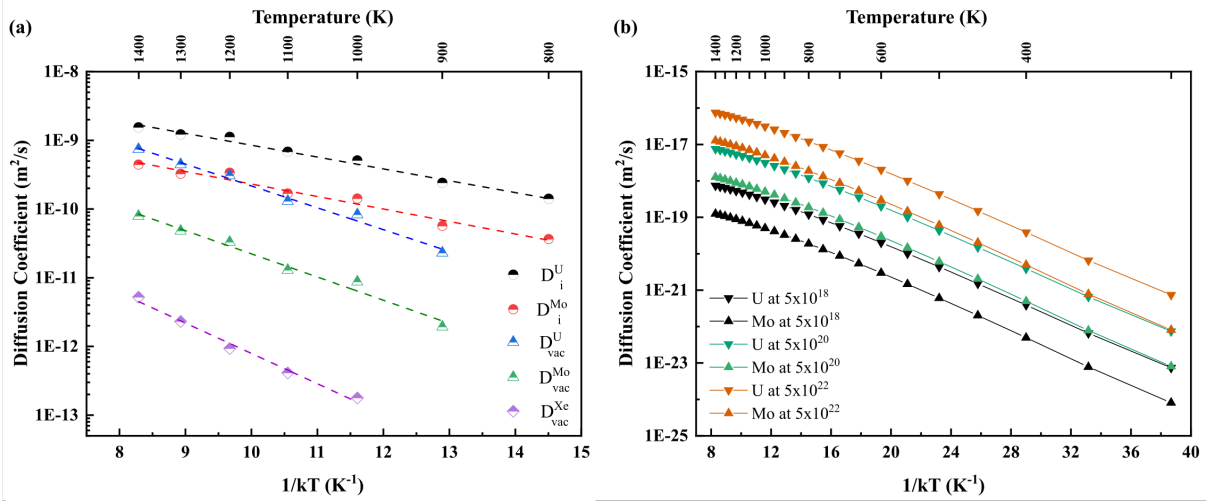


Figure 4: (a) Vacancy and interstitial diffusion coefficients of U, Mo, and Xe. (b) Radiation-enhanced diffusion of U and Mo at three fission rate densities (units are fiss/m³/s).

Table 1: Arrhenius fits of vacancy and interstitial diffusion of U, Mo, and Xe in γ U-10Mo.

| Parameter | Migration energy (eV) | Pre-exponential factor (m ² /s) |
|------------|-----------------------|--|
| D_i^U | 0.40 | 4.49×10^{-8} |
| D_i^{Mo} | 0.42 | 1.52×10^{-8} |
| D_v^U | 0.73 | 3.28×10^{-7} |
| D_v^{Mo} | 0.78 | 5.27×10^{-8} |
| D_v^{Xe} | 1.02 | 2.06×10^{-8} |

fusion of U and Mo, calculated via both experiments and MD simulations, are included for comparison purposes [32, 45]. The intrinsic diffusion calculated using MD simulations [45], is significantly higher than the experimental intrinsic diffusion [32]. The disparity in the intrinsic diffusion, determined via experiments [32] and MD simulations [45], likely originates from the microstructural features. The intrinsic diffusion, calculated via MD simulations, is not affected by the microstructure since the simulations represented an ideal alloy system without defect sinks. Conversely, the experimental results can be influenced by sink features such as dislocations, grain boundaries, and impurities in the alloys, resulting in a decrease in intrinsic diffusion. In addition, in the calculation of intrinsic diffusion using MD simulations [45], there were only three intrinsic diffusion data points for U and Mo above 800 K since diffusion of U and Mo below 800 K was insignificant within the MD timescale. Thus, the extrapolation using three data points at high temperatures may not be a good assumption for lower temperatures. Therefore, the experimental intrinsic diffusion is utilized for comparison to determine the primary diffusion mechanism during research reactor operating conditions.

387

When compared to the experimental intrinsic diffusion [32], the radiation-enhanced diffusion of U and Mo dominated in the intermediate temperature range, depending on the fission rate density. With increasing fission rate densities, the minimum temperature at which radiation-enhanced diffusion dominated increased, and the range of temperatures where radiation-enhanced diffusion is prevalent decreased. Specifically, the radiation-enhanced diffusion of U becomes the primary mode of diffusion between 350 K and 600 K at 5×10^{18} fiss/m³/s (Fig. 5(a)), 450 K and 650 K at 5×10^{20} fiss/m³/s (Fig. 5(b)), and 550 K and 700 K at 5×10^{22} fiss/m³/s (Fig. 5(c)). The radiation-enhanced diffusion of Mo dominated in the temperature ranges between 450 K and [..⁵²] 650 K at 5×10^{18} fiss/m³/s (Fig. 6(a)) and 550 K and 700 K at 5×10^{20} fiss/m³/s (Fig. 6(b)). Above the temperature ranges specified, intrinsic thermal diffusion was dominant, while below this temperature range radiation-driven diffusion was dominant. The [..⁵³] intrinsic thermal diffusion [..⁵⁴] of Mo became faster than the radiation-enhanced diffusion and the radiation-driven diffusion of Mo above 750 K, and the radiation-driven diffusion of Mo became faster than the intrinsic thermal diffusion and the radiation-enhanced diffusion of Mo below 750 K at 5×10^{22} fiss/m³/s (Fig. 6(c)). This decreasing prevalence of radiation-enhanced diffusion with increasing fission rate density is due to the square-root dependency on the fission rate density, while radiation-driven diffusion exhibits a linear dependency on the fission rate density. Thus, the rate of increase of the radiation-driven diffusion with increasing fission rate density surpasses that of radiation-enhanced diffusion. The total diffusion [..⁵⁵] coefficients of U and Mo (including all three diffusion modes) are represented as a function of inverse temperature at three fission rate densities in Fig. 5 (d) and Fig. 6 (d), respectively. [..⁵⁶]

410

[..⁵⁷][..⁵⁸][..⁵⁹]⁵²removed: 600⁵³removed: radiation-enhanced diffusion of Mo exceeded the⁵⁴removed: and the radiation-driven diffusion of Mo only at 750 K at 5×10^{22} fiss/m³/s (Fig. 6(c)). The intrinsic thermal diffusion of Mo⁵⁵removed: of⁵⁶removed: The total diffusion coefficients of U and Mo, respectively, under irradiation can be obtained by the summation of intrinsic thermal diffusion, radiation-enhanced diffusion, and radiation-driven diffusion as follows:

[..⁶⁰][..⁶¹]

[..⁶²]

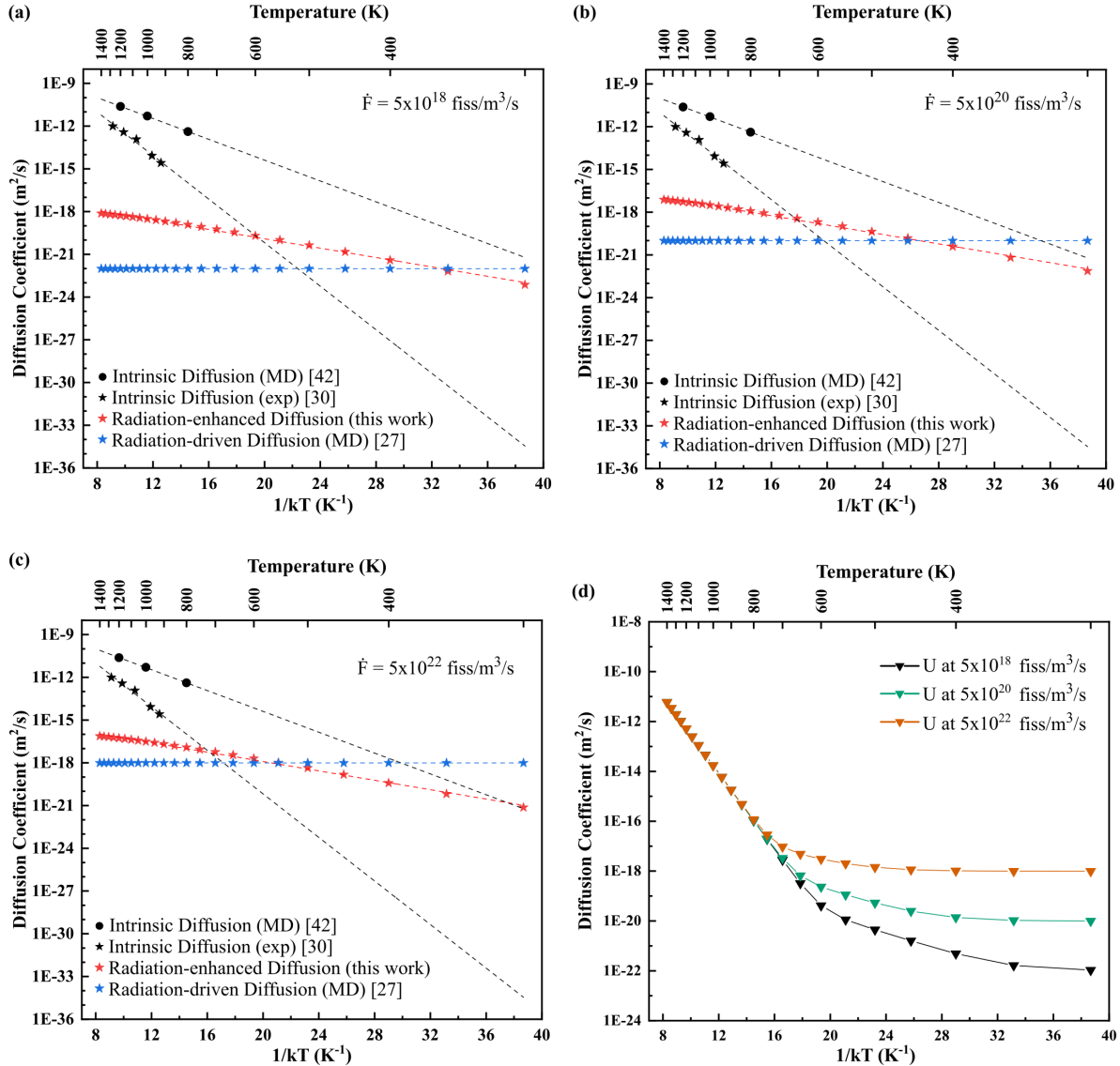


Figure 5: Intrinsic diffusion, radiation-enhanced diffusion, and radiation-driven diffusion of U in γ U-10Mo (a) at $5 \times 10^{18} \text{ fiss}/\text{m}^3/\text{s}$, (b) at $5 \times 10^{20} \text{ fiss}/\text{m}^3/\text{s}$, and (c) at $5 \times 10^{22} \text{ fiss}/\text{m}^3/\text{s}$. (d) Total diffusion of U in γ U-10Mo at three fission rate densities in $\text{fiss}/\text{m}^3/\text{s}$.

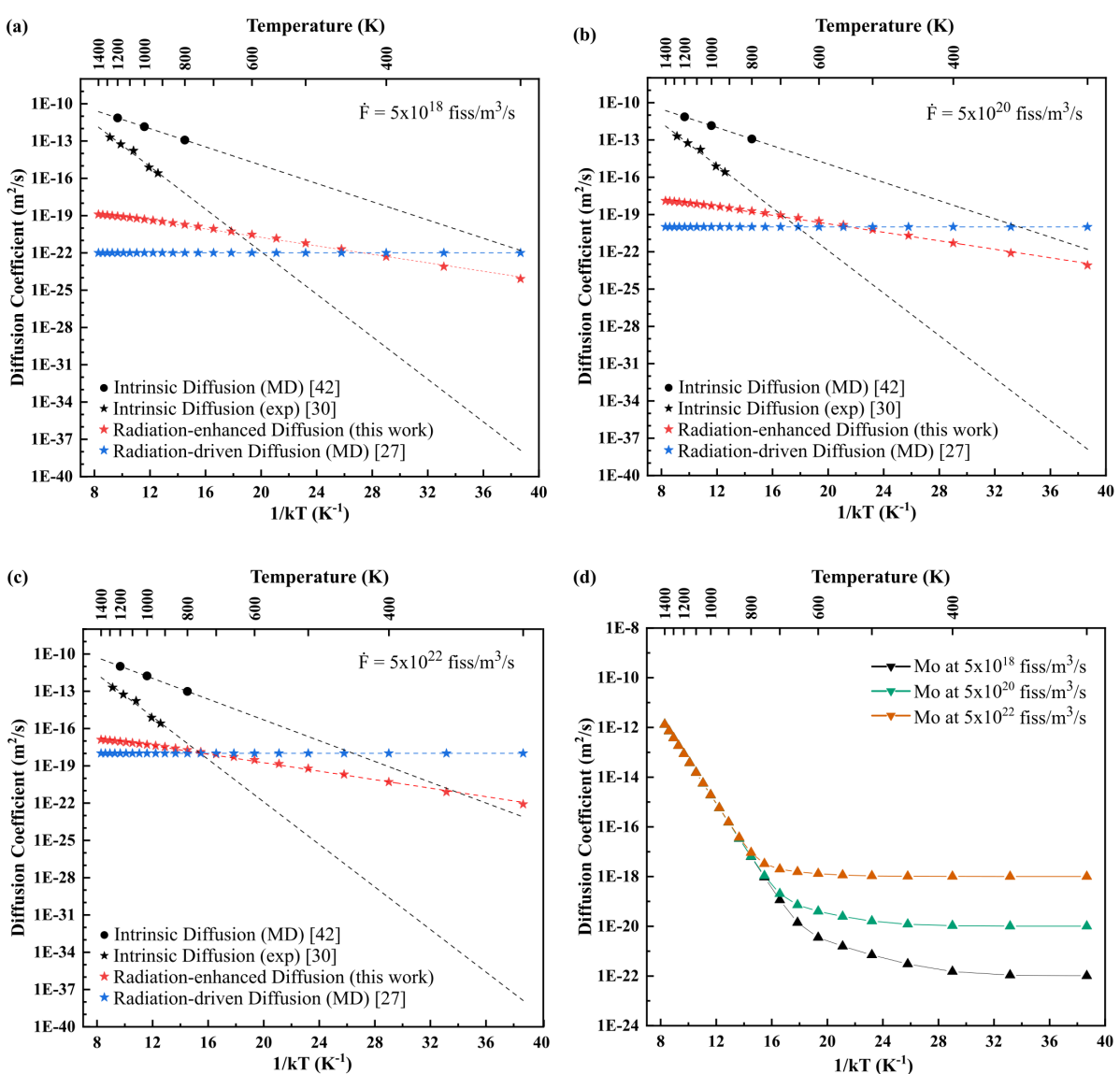


Figure 6: Intrinsic diffusion, radiation-enhanced diffusion, and radiation-driven diffusion of Mo in $\gamma\text{-U-10Mo}$ (a) at $5 \times 10^{18} \text{ fiss}/\text{m}^3/\text{s}$, (b) at $5 \times 10^{20} \text{ fiss}/\text{m}^3/\text{s}$, and (c) at $5 \times 10^{22} \text{ fiss}/\text{m}^3/\text{s}$. (d) Total diffusion of $[_{63}\text{Mo}]$ in $\gamma\text{-U-10Mo}$ at three fission rate densities in $\text{fiss}/\text{m}^3/\text{s}$.

411 3.3. Radiation-enhanced Diffusion of Xe

412 The formation energies of substitutional Xe and Xe-vacancy clusters are calculated as a
 413 function of cluster size and temperature as shown in Fig. 7(a). The formation energies of the
 414 substitutional Xe and the Xe-vacancy clusters increased approximately in a linear fashion
 415 with increasing temperature. The formation energy of each Xe-vacancy cluster was fitted
 416 linearly, and the binding energies were estimated from the fit value of the formation energies.

417 The estimated binding [..⁶⁴] energy of the n^{th} vacancy in a Xe cluster with n vacancies [..⁶⁵]
 418 is represented with respect to the Xe cluster size at 1000 K in Fig. 7(b), where $n = 1$,
 419 2, 3, and 4, as an example. The binding energies of the n^{th} vacancy in a Xe cluster with
 420 n vacancies became higher (more negative) with increasing Xe-vacancy cluster sizes. The
 421 binding energy of a Xe cluster containing more than four vacancies was estimated using a
 422 linear fit at each temperature from 300 K to 1400 K in increments of 50 K.

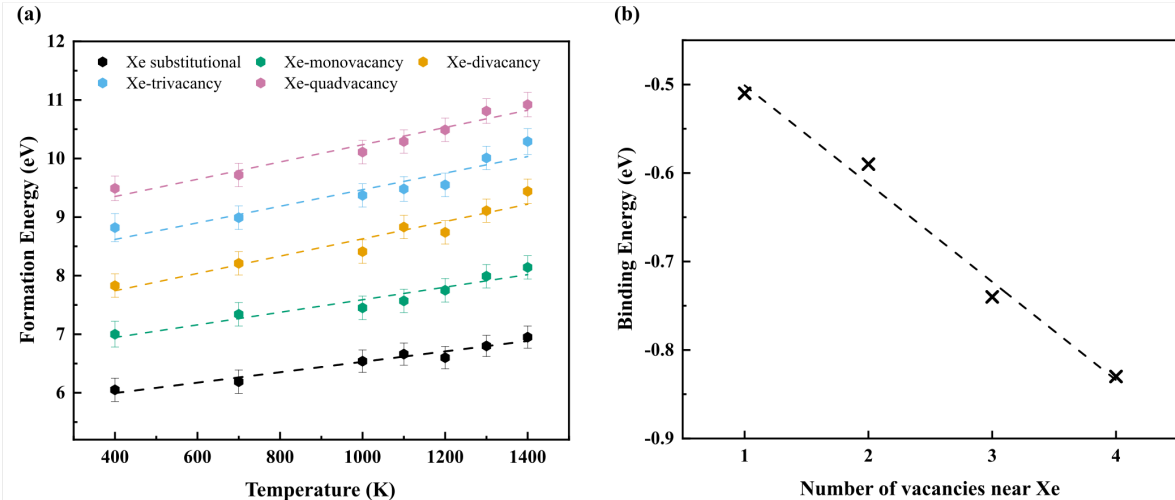


Figure 7: (a) Formation energies of Xe-vacancy clusters as a function of temperature. (b) Binding energies of n^{th} vacancy in a Xe clusters containing n vacancy(ies) at 1000 K, where $n = 1, 2, 3$, and 4 as an example.

423 Given the formation energies and binding energies of all Xe-vacancy clusters of interest,
 424 the absorption and emission coefficients in Eqns. 20 and 21 can be determined and the
 425 rate-theory formulation outlined in Eqns. 13-19 can be implemented. The steady-state con-
 426 centrations of defects, including vacancies, interstitials, Xe substitutionals, and Xe-vacancy
 427 clusters, are calculated as a function of inverse temperature at three fission rate densities in
 428 Fig. 8. [..⁶⁶] The temperature interval was 50 K in the range above 700 K, and the interval
 429 was decreased to 25 K below 700 K to show the smooth transition in the defect concentrations.
 430 The concentration of the Xe clusters including vacancies up to only four (quadvacancy) are
 431 represented for the sake of simplicity in Fig. 8. Complete data of the defect concentrations
 432 with respect to inverse temperature at three different fission rate densities is included in the
 433 Appendix. [..⁶⁷]

434 The steady-state concentrations of Xe-vacancy clusters were dependent on the temper-

⁶⁴removed: energies of

⁶⁵removed: are

⁶⁶removed: It should be noted that the

⁶⁷removed: Defect concentrations at the time of one year were assumed to be steady-state defect concentrations.

435 ature, exhibiting three distinct regimes. In the [..⁶⁸]low-temperature regime, the smallest
 436 Xe-vacancy cluster (the Xe-monovacancy cluster) had the highest concentration, followed by
 437 the Xe-divacancy cluster, the Xe-trivacancy cluster, and the Xe-quadvacancy cluster. This
 438 corresponds to temperatures less or equal to 300 K at 5×10^{18} fiss/m³/s, [..⁶⁹]325 K at 5×10^{20}
 439 fiss/m³/s, and 400 K at 5×10^{22} fiss/m³/s. In the [..⁷⁰]low-temperature regime, there are a
 440 sufficient number of vacancies present to allow for clustering due to the low recombination
 441 rate constant (Fig. 2(b)). However, a small Xe-vacancy cluster is not able to absorb a large
 442 number of vacancies and grow into a bigger vacancy cluster since the diffusion of vacancies
 443 is extremely slow. In the intermediate temperature range, there are still a sufficient number
 444 of vacancies present, and the diffusion of vacancies is sufficiently high to allow for absorption
 445 of vacancies by an existing Xe-vacancy cluster, resulting in the highest concentration of the
 446 biggest Xe-vacancy cluster[..⁷¹]. This intermediate regime corresponds to the temperatures
 447 between [..⁷²]325 K and 500 K at 5×10^{18} fiss/m³/s, 400 K and [..⁷³]575 K at 5×10^{20}
 448 fiss/m³/s, and 450 K and [..⁷⁴]625 K at 5×10^{22} fiss/m³/s. In the [..⁷⁵]high-temperature
 449 regime, the concentration of all of the existing Xe-vacancy clusters started to decrease as
 450 the temperature increased. The population of vacancies was dramatically reduced at high
 451 temperatures due to the high recombination rate constant and the high diffusivity leading to
 452 Frenkel pair annihilation. Thus, there are not enough residual vacancies to interact with the
 453 Xe species. [..⁷⁶]As the temperature increased, the concentration of larger Xe-vacancy clusters
 454 decreased more rapidly than the concentration of smaller Xe-vacancy clusters. As a result,
 455 the concentration of the biggest Xe-vacancy cluster [..⁷⁷]had the lowest concentration, while
 456 the concentration of the smallest Xe-vacancy cluster, Xe-monovacancy cluster, had the high-
 457 est concentration. The [..⁷⁸]high temperature regime corresponds to temperatures greater
 458 than [..⁷⁹]575 K at 5×10^{18} fiss/m³/s, [..⁸⁰]625 K at 5×10^{20} fiss/m³/s, and [..⁸¹]700 K at

⁶⁸removed: low temperature regime

⁶⁹removed: 350

⁷⁰removed: low temperature

⁷¹removed: , followed by the Xe-trivacancy cluster, the Xe-divacancy cluster, and the Xe-monovacancy cluster

⁷²removed: 350

⁷³removed: 550

⁷⁴removed: 650

⁷⁵removed: high temperature

⁷⁶removed: The

⁷⁷removed: , the Xe-quadvacancy cluster,

⁷⁸removed: temperature regime where the smallest cluster had the highest concentration and the biggest cluster had the lowest concentration

⁷⁹removed: or equal to 600

⁸⁰removed: 650

⁸¹removed: 750

459 5×10^{22} fiss/m³/s. Thus, these three [..⁸²]temperature regimes are delineated by changes in
 460 the mobility of vacancies [..⁸³]and the temperature dependence of the recombination rate[..⁸⁴]. It should be emphasized that these trends are applicable for all Xe cluster sizes investigated (up to the [..⁸⁵]Xe-tetradecavacancy cluster), as displayed in Fig. [..⁸⁶]A.1 for clarity.
 462
 463

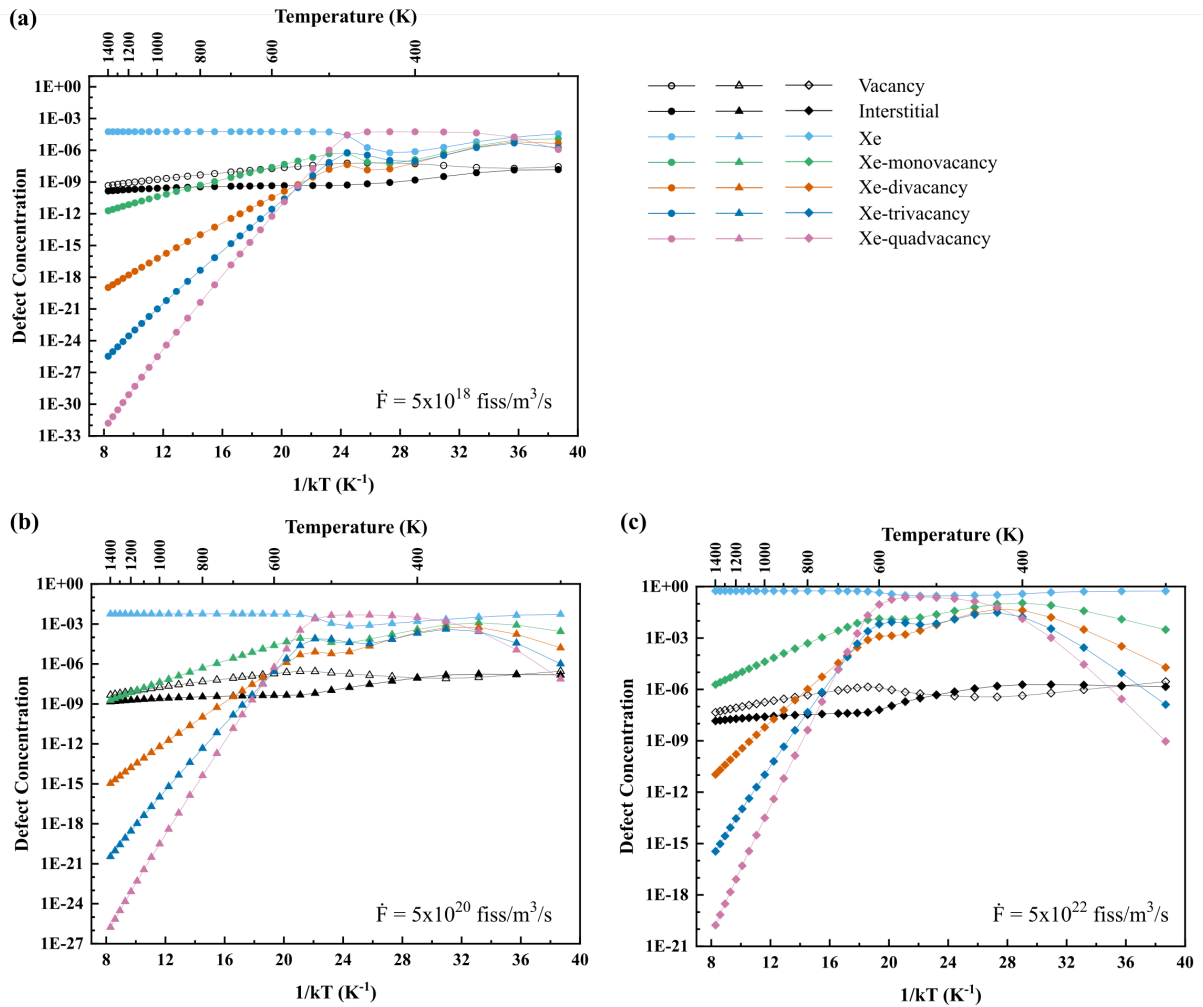


Figure 8: Evolution of defect concentrations in γ U-10Mo as a function of inverse temperature at (a) 5×10^{18} fiss/m³/s, (b) 5×10^{20} fiss/m³/s, and (c) 5×10^{22} fiss/m³/s. Note the differences in the y scales.

464 In order to utilize the Xe-cluster concentrations for Xe radiation-enhanced diffusion cal-
 465 culations in γ U-10Mo, the individual diffusion coefficients of each cluster must be known, as

⁸²removed: temperatures

⁸³removed: ,

⁸⁴removed: , as well as the vacancy and Xe production rate

⁸⁵removed: Xe-quadvacancy

⁸⁶removed: 8

466 outlined in Eqn. [..⁸⁷] 9. The diffusion coefficients of Xe in a vacancy cluster with respect to
467 cluster size and temperature as calculated via MD simulations are represented in Fig. 9(a).
468 The diffusion coefficients of Xe in a vacancy cluster were negligible below 1000 K within the
469 MD timescales. [..⁸⁸] It was expected that the diffusion coefficient of Xe would decrease with
470 increasing vacancy cluster size. However, interestingly, the diffusion coefficients of Xe clusters
471 were effectively independent of the Xe-vacancy cluster size. Due to the insensitivity of the
472 diffusion coefficient on the cluster size, the diffusion coefficient of Xe in a vacancy cluster was
473 obtained by averaging over all cluster sizes at each temperature. The calculated diffusion
474 coefficients were also extrapolated to lower temperatures by fitting to an Arrhenius equation
475 as shown in Fig. 4(a) and Table 1. The Xe-vacancy clusters evaluated in this work were not
476 large enough to be immobile. However, since it is known that a large enough Xe-vacancy clus-
477 ter/bubble is immobile [69, 70], the largest cluster described in this work (Xe-tetradecavacancy)
478 was treated as immobile in the radiation-enhanced diffusion calculations to approximate Xe seg-
479 regation into large bubbles. For example, a 2 nm Xe bubble was found to be immobile in UO₂
480 [69]. Xe clusters containing more than 14 vacancies were not investigated to identify an immobile
481 Xe-vacancy cluster due to the computational expense associated with conducting MD simulations
482 of complex defects for 500 ns.

483 The statistical significance of the diffusion was verified in that linear dependencies of the
484 mean-squared displacement as a function of time were achieved for all clusters, and visual
485 inspection via OVITO [71] was performed to validate the observed results for the mean-
486 squared displacements. Each individual Xe cluster displayed an Arrhenius relationship, albeit
487 with a different pre-factor and migration energy. It is possible that rapid surface diffusion
488 plays a role in the relative mobility of Xe-clusters with a large ($n > 4$) number of vacancies.
489 It should also be noted that only Xe-clusters with a single Xe atom are investigated, and
490 the diffusional behaviors of m Xe- n vacancy ($m > 1$) clusters could be quite different than Xe-
491 vacancy clusters with a single Xe atom. It is presumed that such multi-Xe clusters would
492 diffuse slower than the clusters investigated in this work, and as such the diffusion coefficients
493 within the current study can be considered as an upper bound on the diffusion of possible
494 Xe-vacancy clusters that can form under irradiation.

495 The averaged cluster diffusion coefficients from Fig. 9(a) and the cluster concentrations
496 from Fig. 8 can now be used to calculate the radiation-enhanced diffusion coefficients of Xe
497 in γ U-10Mo. These radiation-enhanced diffusivities are represented with respect to inverse
498 temperature at three fission rate densities in Fig. 9(b). The radiation-enhanced diffusion

⁸⁷removed: ??

⁸⁸removed: Interestingly,

⁴⁹⁹ of Xe is observed to be nearly athermal at high temperatures. Specifically, the athermal
⁵⁰⁰ regime exists at temperatures greater than or equal to 600 K at 5×10^{18} fiss/m³/s, [..⁸⁹
⁵⁰¹] 700 K at 5×10^{20} fiss/m³/s, and [..⁹⁰] 800 K at 5×10^{22} fiss/m³/s. This is attributed to
⁵⁰² the [..⁹¹] decreasing concentration of the smallest Xe-vacancy clusters (Xe-monovacancy),
⁵⁰³ which dominated in this regime, while the diffusion coefficient of Xe in a vacancy cluster
⁵⁰⁴ increased as the temperature increased. These offsetting contributions resulted in a [..⁹²
⁵⁰⁵] near-constant radiation-enhanced diffusion of Xe. In the intermediate temperature regime,
⁵⁰⁶ the radiation-enhanced diffusion of Xe increased with increasing temperature. This was due
⁵⁰⁷ to the increase of the diffusion coefficient of Xe in a vacancy cluster, while the concentration
⁵⁰⁸ of the biggest Xe-vacancy clusters (Xe-quadvacancy), which dominated in this regime, re-
⁵⁰⁹ mained nearly constant. This tendency occurred within the temperature range between 350
⁵¹⁰ K and 600 K at 5×10^{18} fiss/m³/s, [..⁹³] 375 K and 700 K at 5×10^{20} fiss/m³/s, and [..⁹⁴] 400
⁵¹¹ K and 800 K at 5×10^{22} fiss/m³/s. In the [..⁹⁵] low-temperature regime, when compared to
⁵¹² the intermediate temperature regime, the radiation-enhanced diffusion of Xe increased more
⁵¹³ rapidly with increasing [..⁹⁶] temperature since both the diffusion coefficient of Xe and the
⁵¹⁴ concentration of the smallest Xe-vacancy clusters (Xe-monovacancy), which dominated in
⁵¹⁵ this regime, increased. This behavior applied to temperatures less than or equal to [..⁹⁷] 350
⁵¹⁶ K at 5×10^{18} fiss/m³/s, [..⁹⁸] 375 K at 5×10^{20} fiss/m³/s, and 400 K at 5×10^{22} fiss/m³/s.

517

⁸⁹removed: 650

⁹⁰removed: 700

⁹¹removed: deceasing

⁹²removed: near constant

⁹³removed: 400 K and 650

⁹⁴removed: 500 K and 700

⁹⁵removed: low temperature

⁹⁶removed: the

⁹⁷removed: 300

⁹⁸removed: 350

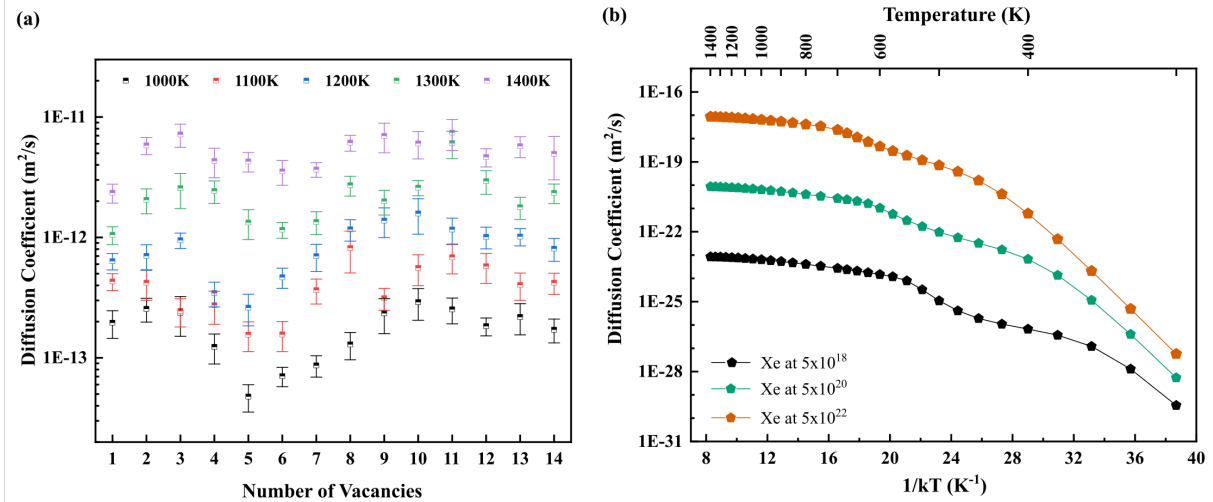


Figure 9: (a) Diffusion coefficient of a Xe-vacancy cluster [..⁹⁹] with respect to size. (b) Radiation-enhanced diffusion of Xe in γ U-10Mo as a function of fission rate density (units are fiss/m³/s).

518 The radiation-enhanced diffusion of Xe is plotted along with the intrinsic thermal diffusion
 519 and radiation-driven diffusion of Xe in Fig. 10 (a)-(c), and the total diffusion coefficient
 520 of Xe under irradiation is represented in Fig. 10(d), all as a function of inverse temperature
 521 at three fission rate densities. It should be noted that the [..¹⁰⁰]intrinsic Xe diffusion coeffi-
 522 cients, both the previously assumed [30, 31] and calculated in this work, are represented in
 523 Fig. 10. The influence of the radiation-enhanced diffusion of Xe on the total diffusion was
 524 dependent on the fission rate density and the intrinsic thermal diffusion of Xe. The intrinsic
 525 thermal diffusion of Xe, calculated in this work, had a higher activation energy [..¹⁰¹] and
 526 was two to ten orders of magnitude slower than the previously assumed intrinsic thermal
 527 diffusion of Xe depending on the temperature (Fig. 10) [30, 31]. The results of the Arrhenius
 528 fits of the intrinsic thermal diffusion of Xe are compared in Table 2. [..¹⁰²]

529 Utilizing the intrinsic thermal diffusion of Xe [..¹⁰³] calculated in this work, the radiation-
 530 enhanced diffusion of Xe at 5×10^{18} fiss/m³/s (Fig. 10(a)) did not significantly contribute
 531 to the total diffusion of Xe at the investigated temperatures. For instance, the radiation-
 532 enhanced diffusion of Xe was approximately [..¹⁰⁴]30-100 times slower than the radiation-
 533 driven diffusion of Xe above [..¹⁰⁵]700 K. The intrinsic thermal diffusion of Xe [..¹⁰⁶] began
 534 to dominate the diffusion processes above 950 K, whereas the radiation-driven diffusion of Xe

¹⁰⁰removed: Xe radiation-enhanced

¹⁰¹removed: ,

¹⁰²removed: When compared to

¹⁰³removed: ,

¹⁰⁴removed: 40-70

¹⁰⁵removed: 600

¹⁰⁶removed: , calculated in this work,

535 began to dominate below 950 K. For the fission rate density of 5×10^{20} fiss/m³/s (Fig. 10(b)),
536 the intrinsic thermal diffusion of Xe [..¹⁰⁷] dominated above 1150 K and the radiation-driven
537 diffusion of Xe dominated below 1150 K. However, the contribution of the radiation-enhanced
538 diffusion of Xe to the total diffusion increased as the fission rate density increased to 5×10^{20}
539 fiss/m³/s (Fig. 10(b)). Specifically, the radiation-enhanced diffusion of Xe was slower than
540 the radiation-driven diffusion of Xe by only a factor of [..¹⁰⁸] 3-10 above 700 K. As the fis-
541 sion rate density increased further to 5×10^{22} fiss/m³/s (Fig. 10(c)), the radiation-enhanced
542 diffusion of Xe exceeded both the intrinsic thermal diffusion [..¹⁰⁹] and the radiation-driven
543 diffusion of Xe at temperatures above [..¹¹⁰] 700 K.

544 The radiation-enhanced diffusion and the radiation-driven diffusion of Xe were also com-
545 pared to the previously [..¹¹¹] utilized intrinsic thermal diffusion of Xe [30, 31]. [..¹¹²] Since
546 this estimate for intrinsic diffusion is significantly faster than the values calculated in this work,
547 the temperature range where intrinsic diffusion becomes dominant occurs at a consistently lower
548 temperature for all fission rate densities. Radiation-enhanced diffusion was not a dominant mode
549 of diffusion for any temperatures for the fission rates of 5×10^{18} [..¹¹³] and 5×10^{20} fiss/m³/s[..¹¹⁴]
550]. As the fission rate density increased further to 5×10^{22} fiss/m³/s (Fig. 10(c)), the radiation-
551 enhanced diffusion of Xe exceeded [..¹¹⁵] the intrinsic thermal diffusion and the radiation-
552 driven diffusion of Xe in the temperature range between [..¹¹⁶] 700 K to 1100 K. Thus, the
553 previously utilized Xe diffusion assumptions underestimate the potential importance of radiation-
554 enhanced diffusion.

555 The differences in the radiation-affected diffusion of U and Mo as compared to Xe are
556 quite stark, especially when considering the respective trends as a function of the fission
557 rate. As mentioned previously, in both U and Mo, a square-root and linear relationship were
558 observed in the radiation-enhanced diffusion and radiation-driven diffusion with respect to
559 fission rate density, respectively. However, in the case of Xe, it becomes more complicated

¹⁰⁷removed: , obtained in this work,

¹⁰⁸removed: 4-7 above 650

¹⁰⁹removed: calculated in this work

¹¹⁰removed: or equal to 750

¹¹¹removed: published

¹¹²removed: Similarly, the radiation-enhanced diffusion of Xe did not significantly contribute to the total diffusion at

¹¹³removed: fiss/m³/s (Fig. 10(a)). However, the previously assumed intrinsic diffusion of Xe became the dominant diffusion process at a lower temperature of 750 K when compared to the intrinsic diffusion calculated in this work. As the fission rate density increased to

¹¹⁴removed: , the previously assumed intrinsic diffusion of Xe dominated above 850 K and the radiation-driven diffusion of Xe dominated below 850 K. However, the radiation-enhanced diffusion of Xe began to contribute to the total diffusion in the temperature range between 650 K and 850 K (Fig. 10(b)).

¹¹⁵removed: both the previously assumed

¹¹⁶removed: 750 K to 1050 K.

due to the interaction of vacancies with Xe and Xe-vacancy clusters, which created non-uniform variability as a function of fission rate density and temperature.

562

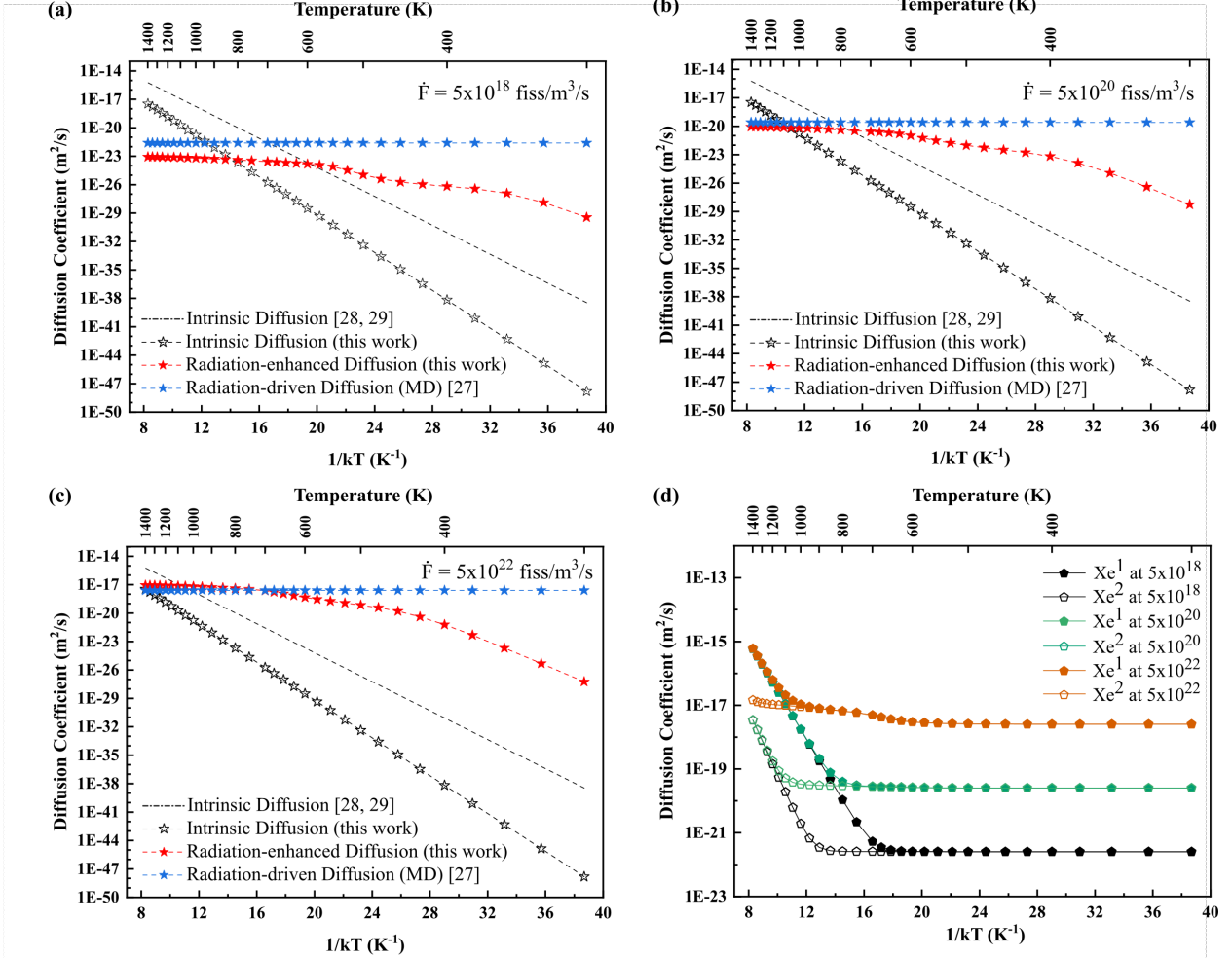


Figure 10: Intrinsic diffusion, radiation-driven diffusion, and radiation-enhanced diffusion of Xe in γ -U-10Mo at (a) $5 \times 10^{18} \text{ fiss}/\text{m}^3/\text{s}$, (b) $5 \times 10^{20} \text{ fiss}/\text{m}^3/\text{s}$, and (c) $5 \times 10^{22} \text{ fiss}/\text{m}^3/\text{s}$. (d) Total diffusion of Xe as a function of fission rate density (fiss/m³/s). Note the differences in the y scales. Xe¹ is calculated from the previous assumption, and Xe² is calculated in this work [30, 31].

Table 2: Arrhenius fit of intrinsic thermal diffusion of Xe in γ -U-10Mo.

| | Activation energy (eV) | Pre-exponential factor (m^2/s) |
|------------------------------|------------------------|--|
| Previous assumption [30, 31] | 1.76 | 1.28×10^{-9} |
| This work | 2.30 | 6.53×10^{-10} |

563 **4. Discussion**

564 Radiation-enhanced diffusion of Xe behaved differently as compared to radiation-enhanced
565 diffusion of U and Mo with respect to temperature and fission rate density in γ U-10Mo. The
566 intrinsic thermal diffusion, radiation-enhanced diffusion, and radiation-driven diffusion of U
567 and Mo dominated in the high, intermediate, and [..¹¹⁷] low-temperature regimes, respec-
568 tively, depending on the fission rate density as described in Section 3.2. Given that the
569 reactor operating temperature is below approximately [..¹¹⁸] 150°C and the fission rate den-
570 sity is on the order of 10^{20} fiss/m³/s in research reactors, both radiation-enhanced diffusion
571 and radiation-driven diffusion of U and Mo contribute to species mobility under irradiation
572 at all relevant research reactor temperatures and fission rate densities [3, 72]. On the other
573 hand, the radiation-enhanced diffusion of Xe did not significantly impact the diffusion under
574 irradiation at relevant temperatures and fission rate densities in research reactors. Alter-
575 nately, radiation-driven diffusion of Xe dominated the diffusion process of Xe for relevant
576 operating conditions in research reactors. For the establishment of future models, the in-
577 trinsic thermal diffusion of each element can likely be neglected in research reactors due to
578 the specific operating parameters (temperature and fission rate density) which dictate the
579 prevalence of irradiation-assisted diffusion.

580 Radiation-enhanced diffusion was previously investigated in other fuel materials such
581 as UO₂ [28, 36] and U₃Si₂ [..¹¹⁹] [37]. In UO₂, it was observed that radiation-enhanced
582 diffusion of Xe dominated over the intrinsic thermal diffusion of Xe below 1561 K at the
583 fission rate density of 10^{19} fiss/m³/s from experiments [26], which is inconsistent with the Xe
584 observations in this work. Anderson et al. [36] predicted the radiation-enhanced diffusion of
585 Xe via cluster dynamics parametrized by DFT and MD simulations, which agreed well with
586 experimental observations. For example, the radiation-enhanced diffusion of Xe dominated
587 over the intrinsic diffusion of Xe below 1771 K at the identical fission rate density in UO₂
588 [26, 36]. In addition, the radiation-enhanced diffusion of U in UO₂ dominated between 1250
589 K and 1800 K at 10^{19} fiss/m³/s [37]. This work established credibility [..¹²⁰] for the prediction
590 of Xe radiation-enhanced diffusion via strictly computational pathways. In the U₃Si₂ system,
591 radiation-enhanced diffusion of U and Si did not significantly contribute to the total diffusion
592 at the evaluated fission rate densities from 10^{17} fiss/m³/s to 10^{19} fiss/m³/s [28], which is in
593 qualitative agreement with the behavior of Xe in this work. The radiation-driven diffusion
594 of U and Si was greater than the radiation-enhanced diffusion of U and Si by 4-5 orders

¹¹⁷removed: low temperature

¹¹⁸removed: 250

¹¹⁹removed: [28, 36, 37]

¹²⁰removed: to

595 of magnitude [28]. Uranium diffusion was faster than Si diffusion, and diffusion occurred
596 primarily via interstitials rather than vacancies in U_3Si_2 [28, 46]. The relative similarities of
597 U-10Mo to the U_3Si_2 system, specifically both having metallic bonding and interstitial-based
598 self-diffusion, suggest that the irradiation-affected diffusion behaviors would also show some
599 similarities, which is confirmed in this work.

600 A comment should be made to contextualize some of the assumptions made, and some of
601 the results observed, in this work. To calculate the radiation-enhanced diffusion of Xe, rate-
602 theory equations (Eqs. 13-19) were constructed to calculate the steady-state concentrations of
603 defects, comprising vacancies, interstitials, Xe, and Xe-vacancy clusters in the fuel under irra-
604 diation. However, unlike the concentrations of vacancies and interstitials, the concentrations of
605 Xe-vacancy clusters did not reach a steady-state value since Xe was continuously produced, and
606 only small Xe-vacancy clusters were considered in the rate-theory equations. Experimentally, it is
607 expected that the concentration of Xe will increase with respect to time under irradiation since
608 Xe is continually produced via fission, but fission gas release does not occur in the U-Mo fuel
609 system. Thus, the concentrations at the time of 45 days, which is approximately the time at
610 which U-10Mo fuel undergoes recrystallization in research reactors, are utilized in the determi-
611 nation of radiation enhanced diffusion of Xe [16, 73, 74, 75, 76]. In addition, the presence of
612 large fission gas bubbles is not explicitly taken into account in the rate-theory equations. Point
613 defects (vacancies and interstitials) and Xe will diffuse into fission gas bubbles, as well as grain
614 boundaries, which are the primary sinks in the fuel, and losses of point defects and Xe will likely
615 decrease the Xe-vacancy cluster concentrations under irradiation. Thus, this work represents an
616 upper bound of the possible radiation-enhanced diffusion of Xe, with a series of assumptions that
617 likely exaggerate the rate at which Xe and Xe-vacancy clusters are able to be transported in
618 U-Mo fuel. This, combined with the limited range of prevalence of radiation-enhanced diffusion
619 for Xe in U-Mo, indicates that it is highly likely that the radiation-driven diffusion of Xe will be
620 the dominant mode of Xe diffusion at temperatures relevant to research reactors.

621

622 5. Summary and Conclusions

623 In the present work, the radiation-enhanced diffusion coefficients of U, Mo, and Xe in
624 $\gamma\text{U}-10\text{Mo}$ were calculated using rate-theory models and MD simulations with the ternary U-
625 Mo-Xe interatomic potential [41] in the temperature range between 300 K and 1400 K and
626 the fission rate density range between $5 \times 10^{18} \text{ fiss}/\text{m}^3/\text{s}$ and $5 \times 10^{22} \text{ fiss}/\text{m}^3/\text{s}$. The calculated
627 radiation-enhanced diffusion coefficient of each element was compared to the intrinsic thermal
628 diffusion and the radiation-driven diffusion, determined previously [29, 32]. The intrinsic
629 thermal diffusion of Xe was calculated using the concentration of vacancies at equilibrium and

the diffusion coefficient of Xe in a monovacancy cluster. The total diffusion of U, Mo, and Xe under irradiation conditions [..¹²¹] were also determined by summing the radiation-enhanced diffusion, calculated in this work, and the previously determined intrinsic thermal diffusion and radiation-driven diffusion [29, 32]. It was found that [..¹²²] both radiation-enhanced diffusion and [..¹²³] radiation-driven diffusion of U and Mo dominated at the operating temperatures and typical fission rate densities [..¹²⁴] of research reactors. The influence of the radiation-enhanced diffusion of Xe on the total diffusion of Xe under irradiation increased with increasing fission rate density. However, the radiation-enhanced diffusion of Xe did not significantly contribute to the total diffusion of Xe at a fission rate density of 5×10^{18} fiss/m³/s and 5×10^{20} fiss/m³/s. The radiation-enhanced diffusion of Xe exceeded the intrinsic diffusion of Xe, calculated in this work, as well as the radiation-driven diffusion of Xe at 5×10^{22} fiss/m³/s above 700 K, although, this is likely beyond the fission rate density regime that is obtained within research reactors. The total diffusion coefficients of U, Mo, and Xe in γ U-10Mo, updated in this work, will be utilized as important parameters in mechanistic fuel models, as well as potentially in other nuclear fuel mesoscale models, such as kinetic Monte Carlo, phase-field models, cluster dynamics, and finite element analysis, to predict the microstructural evolution under irradiation more accurately.

6. CRediT author statement

Gyuchul Park: Conceptualization, Formal analysis, Software, Investigation, Methodology, Visualization, Writing-original draft. **Benjamin Beeler:** Conceptualization, Funding acquisition, Methodology, Project administration, Resources, Supervision, Writing-review and editing. **Maria A. Okuniewski:** Conceptualization, Funding acquisition, Methodology, Project administration, Resources, Supervision, Writing-review and editing.

7. Acknowledgements

This work was supported by the U.S. Department of Energy, Office of Material Management and Minimization, National Nuclear Security Administration, under DOE-NE Idaho Operations Office Contract DE-AC07-05ID14517. This research made use of the [..¹²⁵] High-Performance Computing Center at Idaho National Laboratory, which is supported by the

¹²¹removed: was

¹²²removed: the

¹²³removed: the

¹²⁴removed: typical

¹²⁵removed: High Performance

⁶⁵⁸ Office of Nuclear Energy of the U.S. Department of Energy and the Nuclear Science User
⁶⁵⁹ Facilities.

660 Appendix A.

661 The concentration of vacancies, interstitials, and Xe clusters as a function of inverse
 662 temperature at three fission rate densities is shown in Fig. A.1, including data for all Xe-
 663 vacancy clusters investigated.

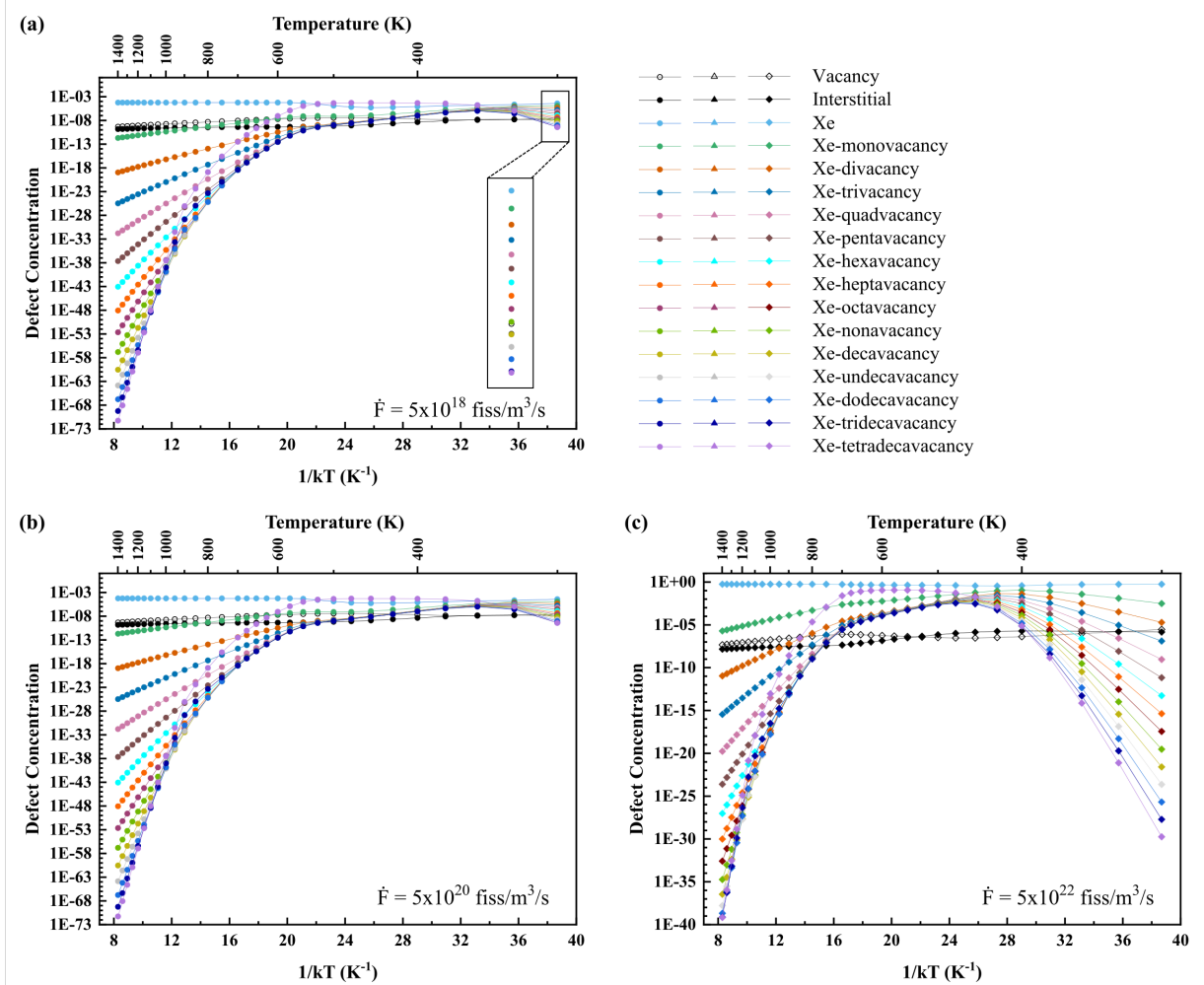


Figure A.1: Evolution of concentrations of vacancies, interstitials, Xe, and Xe-vacancy clusters in γ U-10Mo as a function of inverse temperature at (a) 5×10^{18} fiss/m³/s, (b) 5×10^{20} fiss/m³/s, and (c) 5×10^{22} fiss/m³/s. The Xe-vacancy clusters containing up to 14 vacancies (Xe-tetradecavacancy) are considered.

664 **References**

- 665 [1] Y. S. Kim, G. L. Hofman, Fission product induced swelling of U–Mo alloy fuel, Journal
666 of Nuclear Materials 419 (1–3) (2011) 291–301.
- 667 [2] A. Robinson, D. Perez, D. Porter, et al., Irradiation Performance of U–Mo Alloy Based
668 ‘Monolithic’ Plate-Type-Design Selection Update, Tech. Rep. No. INL/EXT-09-16807,
669 Idaho National Lab.(INL), Idaho Falls, ID (United States) (2013).
- 670 [3] M. Meyer, J. Gan, J. Jue, D. Keiser, E. Perez, A. Robinson, D. Wachs, N. Woolsten-
671 hulme, G. Hofman, Y. Kim, Irradiation performance of U–Mo monolithic fuel, Nuclear
672 Engineering and Technology 46 (2) (2014) 169–182.
- 673 [4] D. Keiser, J.-F. Jue, B. Miller, J. Gan, A. Robinson, J. Madden, Observed changes in
674 as-fabricated U–10Mo monolithic fuel microstructures after irradiation in the advanced
675 test reactor, JOM 69 (12) (2017) 2538–2545.
- 676 [5] R. Prabhakaran, U–Mo monolithic fuel for nuclear research and test reactors, JOM
677 69 (12) (2017) 2529–2531.
- 678 [6] J.-F. Jue, D. D. Keiser Jr, B. D. Miller, J. W. Madden, A. B. Robinson, B. H. Rabin,
679 Effects of irradiation on the interface between U–Mo and zirconium diffusion barrier,
680 Journal of Nuclear Materials 499 (2018) 567–581.
- 681 [7] C. Miller, B. Durtschi, J. I. Cole, K. Daum, U–10Mo Monolithic Fuel Qualification Plan,
682 Tech. Rep. No. INL/EXT-13-30238-Rev003, Idaho National Lab.(INL), Idaho Falls, ID
683 (United States) (2021).
- 684 [8] J. Gan, B. Miller, D. Keiser Jr, J. Jue, J. Madden, A. Robinson, H. Ozaltun, G. Moore,
685 M. Meyer, Irradiated microstructure of U–10Mo monolithic fuel plate at very high fission
686 density, Journal of Nuclear Materials 492 (2017) 195–203.
- 687 [9] J. J. Giglio, USHPRR MP-1: Observations from PIE and path forward for the MP-2
688 Experiment and Experimental Summary, Tech. Rep. No. INL/EXT-21-61324-Rev000,
689 Idaho National Lab.(INL), Idaho Falls, ID (United States) (2021).
- 690 [10] K. Nordlund, S. J. Zinkle, A. E. Sand, F. Granberg, R. S. Averback, R. E. Stoller,
691 T. Suzudo, L. Malerba, F. Banhart, W. J. Weber, F. Willaime, S. L. Dudarev, D. Sime-
692 one, Primary radiation damage: A review of current understanding and models, Journal
693 of Nuclear Materials 512 (2018) 450–479.

- [694] [11] Y. Kim, G. Hofman, J. Rest, G. Shevlyakov, S. RIAR, et al., Characterization of intergranular fission gas bubbles in U-Mo fuel., Tech. Rep. No. ANL-08/11, Argonne National Lab.(ANL), Argonne, IL (United States) (2008).
- [695]
- [696]
- [697] [12] S. Van den Berghe, W. Van Renterghem, A. Leenaers, Transmission electron microscopy investigation of irradiated U-7 wt% Mo dispersion fuel, *Journal of Nuclear Materials* 375 (3) (2008) 340–346.
- [698]
- [699]
- [700] [13] J. Gan, D. D. Keiser Jr, D. M. Wachs, A. B. Robinson, B. D. Miller, T. R. Allen, Transmission electron microscopy characterization of irradiated U-7Mo/Al-2Si dispersion fuel, *Journal of Nuclear Materials* 396 (2-3) (2010) 234–239.
- [701]
- [702]
- [703] [14] D. Olander, D. Wongsawaeng, Re-solution of fission gas—A review: Part I. Intragranular bubbles, *Journal of Nuclear Materials* 354 (1-3) (2006) 94–109.
- [704]
- [705] [15] J. Rest, A model for the effect of the progression of irradiation-induced recrystallization from initiation to completion on swelling of UO_2 and U-10Mo nuclear fuels, *Journal of Nuclear Materials* 346 (2-3) (2005) 226–232.
- [706]
- [707]
- [708] [16] Y. S. Kim, G. Hofman, J. Cheon, Recrystallization and fission-gas-bubble swelling of U-Mo fuel, *Journal of Nuclear Materials* 436 (1-3) (2013) 14–22.
- [709]
- [710] [17] L. Liang, Z.-G. Mei, Y. S. Kim, B. Ye, G. Hofman, M. Anitescu, A. M. Yacout, Mesoscale model for fission-induced recrystallization in U-7Mo alloy, *Computational Materials Science* 124 (2016) 228–237.
- [711]
- [712]
- [713] [18] S. Hu, A. M. Casella, C. A. Lavender, D. J. Senor, D. E. Burkes, Assessment of effective thermal conductivity in U-Mo metallic fuels with distributed gas bubbles, *Journal of Nuclear Materials* 462 (2015) 64–76.
- [714]
- [715]
- [716] [19] T. K. Huber, H. Breitkreutz, D. E. Burkes, A. J. Casella, A. M. Casella, S. Elgeti, C. Reiter, A. B. Robinson, F. N. Smith, D. M. Wachs, et al., Thermal conductivity of fresh and irradiated U-Mo fuels, *Journal of Nuclear Materials* 503 (2018) 304–313.
- [717]
- [718]
- [719] [20] S. Hu, C. H. Henager Jr, H. L. Heinisch, M. Stan, M. I. Baskes, S. M. Valone, Phase-field modeling of gas bubbles and thermal conductivity evolution in nuclear fuels, *Journal of Nuclear Materials* 392 (2) (2009) 292–300.
- [720]
- [721]
- [722] [21] S. Hu, D. E. Burkes, C. A. Lavender, D. J. Senor, W. Setyawan, Z. Xu, Formation mechanism of gas bubble superlattice in UMo metal fuels: Phase-field modeling investigation, *Journal of Nuclear Materials* 479 (2016) 202–215.
- [723]
- [724]

- [22] L. Liang, Z.-G. Mei, Y. S. Kim, M. Anitescu, A. M. Yacout, Three-dimensional phase-field simulations of intragranular gas bubble evolution in irradiated U-Mo fuel, Computational Materials Science 145 (2018) 86–95.
- [23] L. Liang, Y. S. Kim, Z.-G. Mei, L. K. Aagesen, A. M. Yacout, Fission gas bubbles and recrystallization-induced degradation of the effective thermal conductivity in U-7Mo fuels, Journal of Nuclear Materials 511 (2018) 438–445.
- [24] B. Ye, J. Rest, Y. S. Kim, G. Hofman, B. Dionne, DART analysis of irradiation behavior of U-Mo/Al dispersion fuels, Nuclear Technology 191 (1) (2015) 27–40.
- [25] B. Ye, G. Hofman, A. Leenaers, A. Bergeron, V. Kuzminov, S. Van den Berghe, Y. Kim, H. Wallin, A modelling study of the inter-diffusion layer formation in U-Mo/Al dispersion fuel plates at high power, Journal of Nuclear Materials 499 (2018) 191–203.
- [26] J. Turnbull, C. Friskney, J. Findlay, F. Johnson, A. Walter, The diffusion coefficients of gaseous and volatile species during the irradiation of uranium dioxide, Journal of Nuclear Materials 107 (2-3) (1982) 168–184.
- [27] R. Perriot, C. Matthews, M. W. Cooper, B. P. Uberuaga, C. R. Stanek, D. A. Andersson, Atomistic modeling of out-of-pile xenon diffusion by vacancy clusters in UO_2 , Journal of Nuclear Materials 520 (2019) 96–109.
- [28] M. W. D. Cooper, K. A. Gamble, L. Capolungo, C. Matthews, D. Andersson, B. Beeler, C. R. Stanek, K. Metzger, Irradiation-enhanced diffusion and diffusion-limited creep in U_3Si_2 , Journal of Nuclear Materials 555 (2021) 153129.
- [29] B. Beeler, M. W. Cooper, Z.-G. Mei, D. Schwen, Y. Zhang, Radiation driven diffusion in $\gamma\text{U-Mo}$, Journal of Nuclear Materials 543 (2021) 152568.
- [30] S. Hu, V. Joshi, C. Lavender, N. Lombardo, J. Wight, B. Ye, et al., Microstructural level fuel performance modeling of UMo monolithic fuel, Tech. Rep. No. INL/LTD-16-40028, Idaho National Lab.(INL), Idaho Falls, ID (United States) (2016).
- [31] B. Beeler, J. Burks, J. Cole, Y. Gao, G. Hofman, V. Hu, Joshi, C. Lavendar, L. Liang, N. Lombardo, Z.-G. Mei, A. Oaks, J. Wight, A. Yacout, B. Ye, Y. Zhang, Microstructural level fuel performance modeling of UMo monolithic fuel, Tech. Rep. No. INL/LTD-18-51573, Idaho National Lab.(INL), Idaho Falls, ID (United States) (2018).
- [32] K. Huang, J. D. Keiser, Y. Sohn, Interdiffusion, intrinsic diffusion, atomic mobility, and vacancy wind effect in γ (bcc) uranium-molybdenum alloy, Metallurgical and Materials Transactions A 44A (2013) 738.

- 757 [33] M. W. D. Cooper, C. R. Stanek, J. A. Turnbull, B. P. Uberuaga, D. A. Andersson,
758 Simulation of radiation driven fission gas diffusion in UO_2 , ThO_2 and PuO_2 , Journal of
759 Nuclear Materials 481 (2016) 125–133.
- 760 [34] L. Kolotova, S. Starikov, Atomistic simulation of defect formation and structure trans-
761 transitions in U-Mo alloys in swift heavy ion irradiation, Journal of Nuclear Materials 495
762 (2017) 111–117.
- 763 [35] L. Kolotova, S. Starikov, V. Ozrin, Atomistic simulation of the fission-fragment-induced
764 formation of defects in a uranium–molybdenum alloy, Journal of Experimental and
765 Theoretical Physics 129 (1) (2019) 59–65.
- 766 [36] D. Andersson, P. Garcia, X.-Y. Liu, G. Pastore, M. Tonks, P. Millett, B. Dorado, D. Gas-
767 ton, D. Andrs, R. Williamson, et al., Atomistic modeling of intrinsic and radiation-
768 enhanced fission gas (Xe) diffusion in $\text{UO}_{2\pm x}$: Implications for nuclear fuel performance
769 modeling, Journal of Nuclear Materials 451 (1-3) (2014) 225–242.
- 770 [37] C. Matthews, R. Perriot, W. Cooper, C. R. Stanek, D. A. Andersson, Cluster dynamics
771 simulation of xenon diffusion during irradiation in UO_2 , Journal of Nuclear Materials
772 540 (2020) 152326.
- 773 [38] S. Plimpton, Fast parallel algorithms for short-range molecular dynamics, Journal of
774 Computational Physics 117 (1) (1995) 1–19.
- 775 [39] M. S. Daw, M. I. Baskes, Semiempirical, quantum mechanical calculation of hydrogen
776 embrittlement in metals, Physical Review Letters 50 (17) (1983) 1285.
- 777 [40] M. S. Daw, M. I. Baskes, Embedded-atom method: Derivation and application to im-
778 purities, surfaces, and other defects in metals, Physical Review B 29 (12) (1984) 6443.
- 779 [41] D. Smirnova, A. Y. Kuksin, S. Starikov, V. Stegailov, Z. Insepov, J. Rest, A. Yacout,
780 A ternary EAM interatomic potential for U–Mo alloys with xenon, Modelling and Sim-
781 ulation in Materials Science and Engineering 21 (3) (2013) 035011.
- 782 [42] F. Ercolessi, J. B. Adams, Interatomic potentials from first-principles calculations: the
783 force-matching method, EPL (Europhysics Letters) 26 (8) (1994) 583.
- 784 [43] N. Grønbech-Jensen, O. Farago, A simple and effective Verlet-type algorithm for simu-
785 lating Langevin dynamics, Molecular Physics 111 (8) (2013) 983–991.

- [44] N. Grønbech-Jensen, N. R. Hayre, O. Farago, Application of the G-JF discrete-time thermostat for fast and accurate molecular simulations, Computer Physics Communications 185 (2) (2014) 524–527.
- [45] G. Park, B. Beeler, M. A. Okuniewski, An atomistic study of defect energetics and diffusion with respect to composition and temperature in γ U and γ U-Mo alloys, Journal of Nuclear Materials 552 (2021) 152970.
- [46] D. Andersson, X.-Y. Liu, B. Beeler, S. Middleburgh, A. Claisse, C. R. Stanek, Density functional theory calculations of self-and Xe diffusion in U_3Si_2 , Journal of Nuclear Materials 515 (2019) 312–325.
- [47] D. Andersson, B. Uberuaga, P. Nerikar, C. Unal, C. Stanek, U and Xe transport in $UO_{2\pm x}$: Density functional theory calculations, Physical Review B 84 (5) (2011) 054105.
- [48] A. E. Thompson, C. Wolverton, Pathway and energetics of xenon migration in uranium dioxide, Physical Review B 87 (10) (2013) 104105.
- [49] R. Bès, P. Martin, E. Vathonne, R. Delorme, C. Sabathier, M. Freyss, M. Bertolus, P. Glatzel, Experimental evidence of Xe incorporation in schottky defects in UO_2 , Applied Physics Letters 106 (11) (2015) 114102.
- [50] B. Beeler, B. Good, C. Deo, S. Rashkeev, M. Baskes, M. Okuniewski, Formation and incorporation energies of fission gases He, Xe, and Kr in bcc uranium, Minerals, Metals and Materials Society/AIME (2011).
- [51] B. Beeler, B. Good, S. Rashkeev, C. Deo, M. Baskes, M. Okuniewski, First-principles calculations of the stability and incorporation of helium, xenon and krypton in uranium, Journal of Nuclear Materials 425 (1-3) (2012) 2–7.
- [52] B. Beeler, S. Hu, Y. Zhang, Y. Gao, A improved equation of state for Xe gas bubbles in γ U-Mo fuels, Journal of Nuclear Materials 530 (2020) 151961.
- [53] G. Wanner, E. Hairer, Solving ordinary differential equations II, Vol. 375, Springer Berlin Heidelberg New York, 1996.
- [54] J. Bezanson, A. Edelman, S. Karpinski, V. B. Shah, Julia: A fresh approach to numerical computing, SIAM review 59 (1) (2017) 65–98.

- 814 [55] K. Nordlund, S. J. Zinkle, A. E. Sand, F. Granberg, R. S. Averback, R. Stoller,
815 T. Suzudo, L. Malerba, F. Banhart, W. J. Weber, F. Willaime, S. L. Dudarev, D. Sime-
816 one, Improving atomic displacement and replacement calculations with physically real-
817 istic damage models, *Nature Communications* 9 (1) (2018) 1–8.
- 818 [56] M. Norgett, M. Robinson, I. Torrens, A proposed method of calculating displacement
819 dose rates, *Nuclear Engineering and Design* 33 (1) (1975) 50–54.
- 820 [57] B. Beeler, Y. Zhang, M. Okuniewski, C. Deo, Calculation of the displacement energy of
821 α and γ uranium, *Journal of Nuclear Materials* 508 (2018) 181–194.
- 822 [58] Y. Zhang, H. Huang, P. C. Millett, M. Tonks, D. Wolf, S. R. Phillpot, Atomistic study
823 of grain boundary sink strength under prolonged electron irradiation, *Journal of Nuclear*
824 *Materials* 422 (1-3) (2012) 69–76.
- 825 [59] H. Kleykamp, The chemical state of the fission products in oxide fuels, *Journal of*
826 *Nuclear Materials* 131 (2-3) (1985) 221–246.
- 827 [60] A. Nichols, M. Verpelli, D. Aldama, Handbook of nuclear data for safeguards: database
828 extensions, August 2008, IAEA, 2008.
- 829 [61] B. Beeler, J. Cole, W. Frazier, Y. Gao, I. Glagolenko, G. Hofman, S. Hu, V. Joshi,
830 C. Lavendar, N. Lombardo, S. Masengale, Z. Mei, A. Oaks, M. Okuniewski, G. Park,
831 K. Verner, A. Yacout, B. Ye, Y. Zhang, Microstructural-level fuel performance modeling
832 of UMo monolithic fuel, Tech. Rep. No. INL/EXT-20-60591, Idaho National Lab.(INL),
833 Idaho Falls, ID (United States) (2020).
- 834 [62] X.-M. Bai, H. Ke, Y. Zhang, B. W. Spencer, Modeling copper precipitation hardening
835 and embrittlement in a dilute Fe-0.3 at.% Cu alloy under neutron irradiation, *Journal*
836 *of Nuclear Materials* 495 (2017) 442–454.
- 837 [63] G. S. Was, Fundamentals of radiation materials science: metals and alloys, Springer,
838 2016.
- 839 [64] D. Smirnova, A. Y. Kuksin, S. Starikov, Investigation of point defects diffusion in bcc
840 uranium and U–Mo alloys, *Journal of Nuclear Materials* 458 (2015) 304–311.
- 841 [65] K. Yu, Y. Liu, C. Sun, H. Wang, L. Shao, E. Fu, X. Zhang, Radiation damage in
842 helium ion irradiated nanocrystalline Fe, *Journal of Nuclear Materials* 425 (1-3) (2012)
843 140–146.

- 844 [66] K. Nakashima, R. E. Stoller, H. Xu, Recombination radius of a frenkel pair and capture
845 radius of a self-interstitial atom by vacancy clusters in bcc Fe, *Journal of Physics: Condensed Matter* 27 (33) (2015) 335401.
- 846
- 847 [67] M. Veshchunov, A. Boldyrev, A. Kuznetsov, V. Ozrin, M. Seryi, V. Shestak, V. Tarasov,
848 G. Norman, A. Y. Kuksin, V. Pisarev, et al., Development of the advanced mechanistic
849 fuel performance and safety code using the multi-scale approach, *Nuclear Engineering and Design* 295 (2015) 116–126.
- 850
- 851 [68] D. Smirnova, A. Y. Kuksin, S. Starikov, V. Stegailov, Atomistic modeling of the self-diffusion in γ -U and γ -U-Mo, *The Physics of Metals and Metallography* 116 (5) (2015) 445–455.
- 852
- 853
- 854 [69] C. Baker, The migration of intragranular fission gas bubbles in irradiated uranium
855 dioxide, *Journal of Nuclear Materials* 71 (1) (1977) 117–123.
- 856
- 857 [70] D.-U. Kim, S. Blondel, D. E. Bernholdt, P. Roth, F. Kong, D. Andersson, M. R. Tonks,
858 B. D. Wirth, Modeling mesoscale fission gas behavior in UO₂ by directly coupling the
859 phase field method to spatially resolved cluster dynamics, *Materials Theory* 6 (1) (2022)
1–28.
- 860
- 861 [71] A. Stukowski, Visualization and analysis of atomistic simulation data with OVITO—the
862 Open Visualization Tool, *Modelling and Simulation in Materials Science and Engineering* 18 (1) (2009) 015012.
- 863
- 864 [72] M. A. Marshall, M. A. Lillo, New As-run Neutronics Analysis for RERTR-12 Fuel Foil
865 Experiments, Tech. Rep. No. INL/CON-15-36359-Rev000, Idaho National Lab.(INL),
Idaho Falls, ID (United States) (2016).
- 866
- 867 [73] A. Leenaers, W. Van Renterghem, S. Van den Berghe, High burn-up structure of U(Mo)
dispersion fuel, *Journal of Nuclear Materials* 476 (2016) 218–230.
- 868
- 869 [74] D. Perez, M. Lillo, G. Chang, N. Woolstenhulme, RERTR-12 Insertion 1 Irradiation
870 Summary Report, Tech. Rep. No. INL/EXT-11-24101IN, Idaho National Lab.(INL),
Idaho Falls, ID (United States) (2012).
- 871
- 872 [75] D. Perez, G. Chang, D. Wachs, G. Roth, N. Woolstenhulme, RERTR-12 Insertion
873 2 Irradiation Summary Report, Tech. Rep. No. INL/EXT-12-27085, Idaho National
Lab.(INL), Idaho Falls, ID (United States) (2012).

⁸⁷⁴ [76] C. A. Smith, S. Biswas, B. D. Miller, B. Kombaiah, D. Frazer, D. D. Keiser,
⁸⁷⁵ A. Aitkaliyeva, High burnup structure formation in U-Mo fuels, Journal of Nuclear
⁸⁷⁶ Materials 563 (2022) 153617.